

# Sensitivity analysis and uncertainty quantification of 1-D models of pulmonary hemodynamics in mice under control and hypertensive conditions

Mitchel J. Colebank  | M. Umar Qureshi | Mette S. Olufsen 

Department of Mathematics, North Carolina State University, Raleigh, North Carolina

#### Correspondence

Mette S. Olufsen, Department of Mathematics, North Carolina State University, Raleigh, NC.  
 Email: msolufse@ncsu.edu

#### Present Address

Mette Olufsen Department of Mathematics NC State University Raleigh NC 27695

#### Funding information

American Heart Association, Grant/Award Number: 19PRE34380459;  
 National Science Foundation, Grant/Award Numbers: 1246991 and 1615820

#### Abstract

Pulmonary hypertension (PH), defined as an elevated mean blood pressure in the main pulmonary artery (MPA) at rest, is associated with vascular remodeling of both large and small arteries. PH has several sub-types that are all linked to high mortality rates. In this study, we use a one-dimensional (1-D) fluid dynamics model driven by *in vivo* measurements of MPA flow to understand how model parameters and network size influence MPA pressure predictions in the presence of PH. We compare model predictions with *in vivo* MPA pressure measurements from a control and a hypertensive mouse and analyze results in three networks of increasing complexity, extracted from micro-computed tomography (micro-CT) images. We introduce global scaling factors for boundary condition parameters and perform local and global sensitivity analysis to calculate parameter influence on model predictions of MPA pressure and correlation analysis to determine a subset of identifiable parameters. These are inferred using frequentist optimization and Bayesian inference via the Delayed Rejection Adaptive Metropolis (DRAM) algorithm. Frequentist and Bayesian uncertainty is computed for model parameters and MPA pressure predictions. Results show that MPA pressure predictions are most sensitive to distal vascular resistance and that parameter influence changes with increasing network complexity. Our outcomes suggest that PH leads to increased vascular stiffness and decreased peripheral compliance, congruent with clinical observations.

#### KEYWORDS

computational fluid dynamics, network models, pulmonary hypertension, sensitivity analysis, uncertainty quantification

## 1 | INTRODUCTION

Pulmonary hypertension (PH) is defined as a mean pulmonary arterial blood pressure greater than or equal to 25 mmHg at rest and encompasses five main etiologies, all of which lead to right heart failure if untreated.<sup>1</sup> PH patients experience vascular remodeling in both large and small vessels, leading to increased pulmonary arterial blood pressure and an elevated ventricular afterload, the external stress that the heart must overcome to eject blood into the main pulmonary artery (MPA). These changes consequently alter the type, magnitude, speed, and arrival time of local pressure and flow

waves.<sup>2,3</sup> PH has no cure and is only diagnosed after an initial screening by echocardiogram and invasive measurement of pulmonary arterial blood pressure via right heart catheterization, resulting in delayed diagnosis of the disease and limited treatment options.<sup>1</sup> The objective of this study is to understand how changes in network complexity (obtained from micro-computed tomography (micro-CT) imaging) and vessel stiffness impact predictions of MPA blood pressure in PH. To do so, we use a one-dimensional (1-D) fluid dynamics model as it enables us to understand how pathology impacts the vascular structure (e.g., wall stiffness and network morphology) and function (e.g., blood pressure and flow propagation), which is vital for developing better clinical tools for disease detection and monitoring.<sup>4,5</sup> To test the fidelity of our model, we use sensitivity analysis, uncertainty quantification, and parameter inference comparing model predictions with MPA pressure data measured in mice under control and hypertensive (induced by hypoxia) conditions.

1-D fluid dynamics models require specification of four components, including (a) the geometry of the vascular network, (b) a 1-D approximation of the Navier-Stokes equations, satisfying conservation of mass and balance of axial momentum, (c) a constitutive equation relating transmural pressure and vessel cross-sectional area, and (d) inlet, outlet, and junction conditions. Numerous studies have used 1-D models to investigate wave propagation in the systemic circulation<sup>3,6-10</sup> and to study how changes in vascular wall mechanics impact systemic hemodynamics.<sup>11-13</sup> While a majority of studies are carried out in the systemic circulation, several recent works have analyzed dynamics in the pulmonary circulation.<sup>14-17</sup> For example, Qureshi et al<sup>16</sup> developed a 1-D model connecting pulmonary arteries and veins, while Lee et al<sup>14</sup> and Qureshi et al<sup>17</sup> studied nonlinearity of the pulmonary arterial wall deformation.

The 1-D model can describe hemodynamics in both the systemic and pulmonary systems, though the systems differ significantly. The systemic network distributes blood via long vessels, forming a specialized network reaching all organs in the body, except the lungs, under a high mean pressure gradient changing from about 92 mmHg in the aorta to approximately 2 mmHg in the capillaries.<sup>18</sup> In contrast, the pulmonary system transports blood from the right ventricle to the left atrium, covering a relatively short distance via a rapidly branching network of highly compliant vessels, see Figure 1. The pulmonary system transports blood under a lower mean pressure gradient, from about 15 mmHg in the MPA to approximately 2 mmHg in the pulmonary veins.<sup>18</sup> These fundamental differences between the structure and function of the two systems significantly impact the parameter ranges and model behavior needed for hemodynamic predictions; a question not addressed in previous studies. A better understanding of how the model parameters impact hemodynamic predictions, i.e., the model sensitivity to parameters, is important for understanding the rapid progression of PH and eventual right heart failure. In this study, we use sensitivity analysis and uncertainty quantification to address key questions related to these aspects.

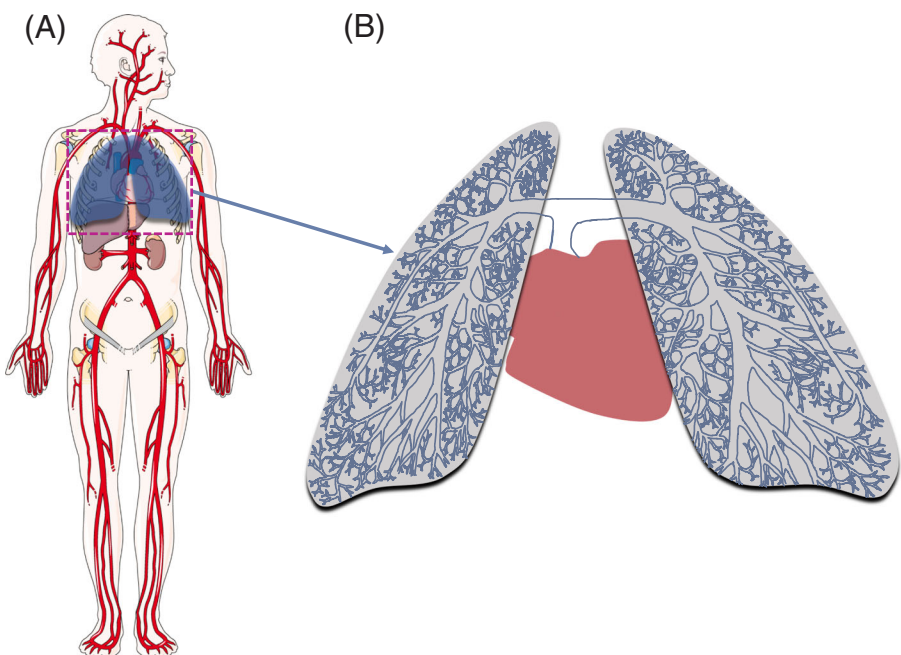


**FIGURE 1** Physiological diagram illustrating (A) the systemic arterial circulation in humans compared with (B) the pulmonary circulation in the lung. The pulmonary circulation begins with the main pulmonary artery (MPA) and bifurcates into the left and right pulmonary arteries, quickly bifurcating afterwards throughout the lungs

Sensitivity analysis quantifies the effects of model parameters on simulated quantities of interest by systematically perturbing parameters and quantifying their effects. This analysis can be conducted using either local<sup>19,20</sup> or global<sup>21–23</sup> methods, providing parameter rankings<sup>20,24</sup> and time-varying sensitivities.<sup>25–27</sup> Local sensitivity metrics are computed from explicit sensitivity equations<sup>20</sup> or approximated using finite differences,<sup>23,28</sup> automatic differentiation,<sup>20,29</sup> or complex step methods.<sup>23,30</sup> Local methods are computationally inexpensive but are only guaranteed to be valid at a given parameter value if the model is linear.<sup>22</sup> In contrast, global methods approximate the model sensitivity throughout a specified parameter space,<sup>22,23,31,32</sup> albeit at a much higher computational cost. Global sensitivity analysis can be conducted using variance-based methods, such as Sobol' indices<sup>22,32</sup> or Morris screening.<sup>21</sup> Sobol' indices provide a more robust, finer measure of parameter influence, whereas Morris screening provides a coarse approximation of the global sensitivities. While the Sobol' methods perform a more extensive analysis over the entire parameter space, screening methods are less computationally expensive and are in good agreement with total indices obtained from Sobol' indices.<sup>31</sup>

A thorough sensitivity analysis is of particular importance for network models, as the extent of the network used affects both the number of parameters in the system and their respective influence on model predictions.<sup>14,33–35</sup> The effects of changing parameters in large network models are nonlinear and intricate, largely due to the complex physics of the system.<sup>19,36</sup> Moreover, the physiological range for each parameter depends on both the network topology and the disease state. To address this problem, it is important to understand how the model sensitivity changes with network size and if it is possible to infer parameters given the available data. Several recent studies<sup>19,37,38</sup> have conducted sensitivity analyses and examined uncertainties in predictions for a range of cardiovascular models.<sup>26,27,39–42</sup> Two studies<sup>26,43</sup> have quantified how parameter influence changes with network size and complexity, and one study<sup>39</sup> has examined time-varying changes in model sensitivities. To our knowledge, no previous studies have examined the sensitivity of model predictions to parameters in pulmonary arterial networks, which may shed more light on differences between the systemic and pulmonary systems and assist in understanding differences between the more prevalent essential systemic hypertension and the relatively rare, yet less understood, PH.

MPA blood pressure, a signature of pulmonary hemodynamics, is vital for PH diagnosis, making it an ideal quantity of interest for sensitivity analysis. Changes in MPA pressure are attributed to proximal and distal vascular resistance and pulmonary vascular compliance,<sup>1,17</sup> which serve as biomarkers for disease progression. Ideally, parameter inference would identify biomarkers using the model and available data; however, limited PH patient data leads to a naturally ill-posed inverse problem. To mitigate this, we introduce global scaling factors<sup>17,44</sup> to simultaneously adjust nominal parameter estimates and reduce the parameter space by removing correlated parameters.<sup>20,24,45</sup> Once the parameter set is reduced, parameter inference is done using both frequentist and Bayesian methods. The former methods treat parameters as fixed and are less computationally expensive, while the latter treat parameters as random variables, allowing for calculation of parameter posterior distributions using numerous Monte Carlo samples.<sup>23,44</sup> Once parameters are inferred, frequentist and Bayesian uncertainty quantification methods are used for both the parameters and model output, providing a measure of model robustness to natural variation in parameters and measurement error.

Our objective is to analyze the sensitivity and uncertainty of MPA pressure predictions from 1-D fluid dynamics models in networks of varying complexity. We perform our analysis using data from two different mice under control and hypoxic environments, the latter inducing PH. We hypothesize that it is essential to include several vessels in the network to obtain sufficiently accurate physiological information. To test our hypothesis, we compare predictions in three different networks: a single vessel model containing the MPA, a slightly more complex three-vessel network, and a more realistic network with 21 vessels. The latter is chosen as it is the largest number of vessels that can be uniquely identified in both the control and hypoxic mouse. We introduce a reduced parameter subset using a scaling factor approach<sup>17</sup> and conduct sensitivity analyses to quantify the parameters' influence on pressure predictions in the MPA. We compute sensitivities using local, derivative-based,<sup>20,45</sup> and global screening methods<sup>21</sup> and investigate how sensitivity metrics change over the cardiac cycle and with network size. We use correlation analysis and posterior parameter pairwise plots from Markov chain Monte Carlo (MCMC) sampling to determine identifiable parameters, which are inferred by minimizing the least squares error between measured and computed MPA pressure. Finally, we quantify uncertainty of the inferred parameters using asymptotic frequentist analysis, and the Delayed Rejection Adaptive Metropolis (DRAM) algorithm and propagate this uncertainty forward to compute confidence, credible, and prediction intervals for simulated waveforms.<sup>45,46</sup> The workflow for this process is shown in Figure 2.

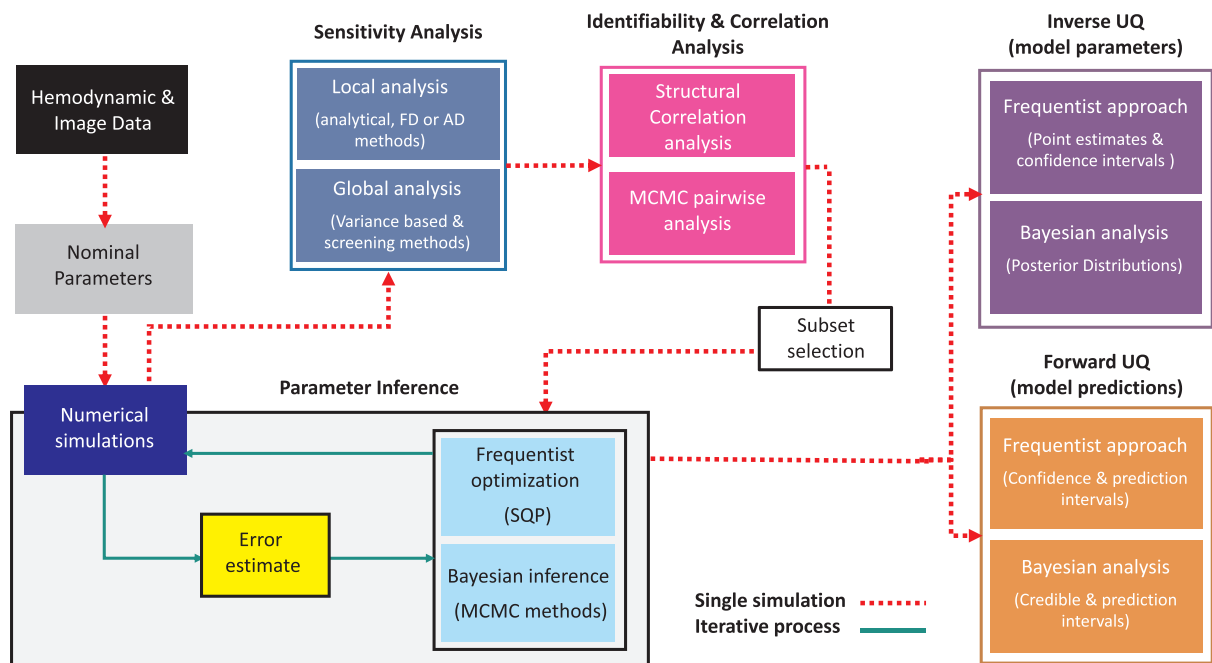


**FIGURE 2** General workflow of the data analysis process. Abbreviations: DRAM, Delayed Rejection Adaptive Metropolis; MCMC, Markov chain Monte Carlo; SQP, sequential quadratic programming; UQ: uncertainty quantification

## 2 | METHODS

### 2.1 | Data

This study uses *in vivo* hemodynamic and micro-CT imaging data from control and hypoxic mice. Detailed experimental protocols describing this data can be found in previous studies.<sup>47,48</sup> All experimental procedures are approved by the University of Wisconsin Institutional Animal Care and Use Committee. Below is a brief summary of the experimental protocol and the methods for network construction.

#### 2.1.1 | Hemodynamic and imaging data

The hemodynamic data include ensemble-averaged MPA pressure and flow waveforms gated to the electrocardiogram (ECG) fiducial point.<sup>47</sup> Blood pressure is measured at a rate of 5 kHz using a 1.0-F pressure-tip catheter (Millar Instruments, Houston, TX) and the flow, measured with ultrasound, is sampled at 30 MHz. We examine data from one control and one hypoxic adult male C57BL6/J mouse (12-13 weeks, weight 24 g), selected from groups of seven control and five hypoxic mice. The latter specimen is subject to a hypoxic environment for 21 days, thus creating hypoxia-induced PH in the mouse. For each group (control and hypoxia), the mice with hemodynamics closest to the group average are used for analysis in this study. The flow waveform is recorded at the inlet of the MPA, while MPA pressure is recorded proximal to the first bifurcation in the network. For computations, we assume that the pressure data corresponds to the predictions in the midpoint of the vessel.

The imaging data include stacked planar X-ray micro-CT images of pulmonary arterial trees from two male C57BL6/J mice, selected from groups of four control and four hypoxic mice (10-12 weeks, weight 24 g). The hypoxic mice used for the imaging study were subject to a hypoxic environment for 10 days. The pulmonary arterial trees are imaged under a static filling pressure of 6.3 mmHg while rotating the lungs in an X-ray beam at 1° increments to obtain 360 planar images. The Feldkamp cone-beam algorithm<sup>49</sup> is used to render the isometric 3-D volumetric dataset (497 × 497 × 497 pixels) by reconstructing and converting the 360 planar images into DICOM 3.0. See Vanderpool et al<sup>34</sup> for more details on animal preparation, handling, and experimental setup and Karau et al<sup>34</sup> for details on the micro-CT image acquisition.

## 2.1.2 | Network geometry

Similar to our previous studies,<sup>17,44</sup> networks are extracted from Digital Imaging and Communications in Medicine (DICOM) images. We use ITK-SNAP<sup>50</sup> to segment the images and render 3-D structures and Paraview (Kitware; Clifton Park, NY) to convert segmentations to Visualization ToolKit Polygonal (vtpl) files. Lastly, the 3-D networks are converted to data structures containing centerline coordinates, vessel radii, and orientation using the Vascular Modeling Toolkit (VMTK).<sup>51,52</sup>

We use a custom MATLAB (Mathworks; Natick, MA) algorithm to construct a 1-D graph representation of the network, described by a connectivity matrix linking edges (vessels) and nodes (junctions). Each edge is associated with a series of xyz-coordinates denoting points along the centerline and their corresponding radii. The radius for each edge is calculated by averaging the center 80% of the vessel radii,<sup>17</sup> and the length  $L$  is calculated as the sum of the distances between xyz-coordinates ( $\mathbf{x}_i$ ), giving

$$r_0 = \frac{1}{N_v} \sum_{i=1}^{N_v} r_i, \quad L = \sum_{i=1}^M l_i, \quad \text{where} \quad l_i = \|\mathbf{x}_{i+1} - \mathbf{x}_i\|, \quad (1)$$

$M$  is the number of points along the vessel centerline and  $N_v$  is the center 80% of the points. Junction points (nodes) corresponding to vessel bifurcations are identified as the intersection between two centerlines and embedded in a connectivity matrix.

Hemodynamic data is only available from the MPA; hence, the simplest fluid dynamics model includes a single vessel (SV) model (left panel of Figure 3) emanating at the root of the pulmonary vasculature and terminating at the first pulmonary junction. We compare results in the SV model with the second smallest network containing three vessels, the MPA and the left and right pulmonary arteries, (center panel in Figure 3). We refer to this model as the “single bifurcation” (SB) model. The advantage of the SB model is that it can predict perfusion to the left and the right lobes of the lung, enabling us to compare results with previous studies.<sup>4,16</sup> Lastly, we compare results from the SV and SB networks with a more realistic network containing 21 vessels (right panel of Figure 3). We include 21 vessels as it is the largest number of vessels that can be identified in both the control and hypoxic animals, i.e., the two networks have the same connectivity, but the vessel radii and lengths (given in Table 1) vary. This allows for comparison between disease states without considering the influence of connectivity. Given that the three models are of various size, we can account for the effects of model-induced wave reflections, which are prominent in larger network models.<sup>27</sup> Moreover, the 21-vessel model allows us to analyze the role attributed to changes in distal vessel segments on PH progression.<sup>1,14,15,53</sup> Ideally, we should gradually

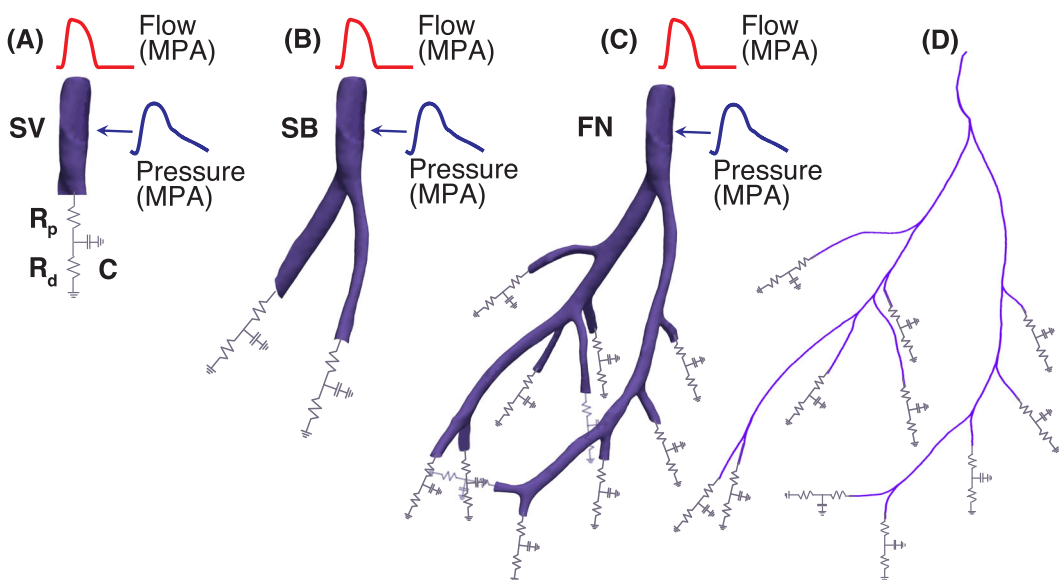


**FIGURE 3** Pulmonary arterial networks constructed from micro-computed tomography (micro-CT) images of a control mouse. Three models are analyzed: (A) a single vessel model (SV), (B) a single bifurcation model (SB), and (C) a 21-vessel full network model (FN). The 1-D model (D) is constructed by extracting centerlines from an isometric 3-D volumetric surface rendered from the segmented images. The networks are represented by a connectivity matrix with nodes, edges, vessel radii, lengths, and orientation. A flow waveform obtained from data is attached at the network inlet, and at the outlets we, attach three-element Windkessel models, relating flow and pressure. Pressure data is measured at the midpoint of the MPA and used for parameter inference

**TABLE 1** Vessel dimensions and connectivities for SV, SB, and FN networks for the control and hypoxic mice

Vessel Index	Connectivity (Daughters)	Control		Hypoxic	
		$r_0 \times 10^{-1}$ (cm)	$L \times 10^{-1}$ (cm)	$r_0 \times 10^{-1}$ (cm)	$L \times 10^{-1}$ (cm)
1 <sup>a,b</sup>	(2,3)	0.47	4.10	0.51	3.58
2 <sup>b</sup>	(4,5)	0.26	4.45	0.26	4.03
3 <sup>b</sup>	(6,7)	0.37	3.72	0.37	3.08
4	(8,9)	0.24	2.41	0.25	2.92
5	–	0.13	0.52	0.17	0.65
6	(14,15)	0.32	2.02	0.28	1.60
7	–	0.17	2.12	0.19	0.93
8	(10,11)	0.23	3.11	0.24	2.06
9	–	0.17	1.77	0.17	0.51
10	(12,13)	0.20	2.62	0.22	2.37
11	–	0.16	0.69	0.17	0.88
12	–	0.15	1.40	0.19	1.27
13	–	0.14	0.62	0.15	0.51
14	(16,17)	0.26	0.81	0.27	1.20
15	–	0.19	1.84	0.19	1.55
16	(18,19)	0.25	0.83	0.26	0.71
17	–	0.15	3.02	0.18	1.68
18	(20,21)	0.24	4.69	0.24	3.55
19	–	0.15	1.77	0.18	1.86
20	–	0.22	1.78	0.23	2.24
21	–	0.18	0.55	0.19	1.07

Note. For each connectivity pair  $(i,j)$ ,  $i$  refers to the left and  $j$  to the right daughter. Vessels marked with – are terminal.

Abbreviations: FN, full network; SB, single bifurcation; SV, single vessel.

<sup>a</sup>Dimensions for the SV model.

<sup>b</sup>Dimensions for the SB model.

increase the network from 3 to 21 vessels; however, the computational cost associated with parameter inference and UQ is expensive, requiring several thousands of forward simulations for each model and disease type. Therefore, we limit our analysis to the three networks, shown in Figure 3: (a) a single-vessel (SV - zero bifurcation) model, (b) a three-vessel (SB) model, and (c) a 21-vessel (full network [FN], 10 bifurcations) model.

## 2.2 | Modeling

Similar to previous studies,<sup>15-17</sup> the 1-D fluid dynamics model is derived from the continuity and Navier-Stokes equations combined with a constitutive equation relating pressure and vessel area. A measured flow waveform is prescribed at the inlet of the MPA, and outlet boundary conditions are specified by three-element Windkessel models, with nominal parameter values calculated using the hemodynamic data and network geometry.

### 2.2.1 | 1-D fluid dynamics equations

The 1-D model is derived under the assumptions that the vessels are cylindrical, blood is incompressible, flow is Newtonian, laminar, and axisymmetric (with no swirl), and that the arterial walls are impermeable. The equations for mass conservation and momentum balance are written as<sup>8,15-17</sup>

$$\frac{\partial A}{\partial t} + \frac{\partial q}{\partial x} = 0, \quad \frac{\partial q}{\partial t} + \frac{\partial}{\partial x} \left( \frac{q^2}{A} \right) + \frac{A}{\rho} \frac{\partial p}{\partial x} = -\frac{2\pi\nu r}{\delta} \frac{q}{A}, \quad (2)$$

where  $x$  (cm) and  $t$  (s) denote the axial and temporal coordinates,  $p(x,t)$  (mmHg) denotes the transmural blood pressure,  $q(x,t)$  (ml/s) the volumetric flow rate, and  $A(x,t)=\pi r(x,t)^2(\text{cm}^2)$  is the cross-sectional area, where  $r(x,t)$  (cm) is the vessel radius. The blood density  $\rho$  (g/ml), kinematic viscosity  $\nu$  (cm<sup>2</sup>/s), and boundary layer thickness  $\delta$  (cm) are assumed constant. The momentum equation is derived under the no-slip condition, satisfied by imposing a flat velocity profile over the lumen area<sup>8</sup> with a thin boundary layer that decreases linearly in the vicinity of the walls, where the transition to no-slip takes place. In order to maintain consistent units in the system of Equations 2, we convert the pressure from mmHg to units of (g/(cm s<sup>2</sup>)) using the conversion factor 1 mmHg = 1333.22 (g/(cm s<sup>2</sup>)).

To close the system, we adopt a constitutive equation relating pressure and cross-sectional area via a linear wall model.<sup>54</sup> The wall model is derived under the assumptions that the vessels are cylindrical and that the walls are thin ( $h/r_0 \ll 1$ ), incompressible, homogeneous, and orthotropic.<sup>55</sup> We assume that the loading and deformation are axisymmetric and that the vessels are tethered in the longitudinal direction so that longitudinal strain is negligible. Under these conditions, the external force reduces to stress in the circumferential direction, yielding a linear stress-strain relation

$$p = \beta \left( \sqrt{\frac{A}{A_0}} - 1 \right), \quad \beta = \frac{Eh}{(1-\kappa^2)r_0}, \quad (3)$$

where  $\beta$  (mmHg) denotes the vessel stiffness.  $E$  (mmHg) denotes the circumferential Young's modulus,  $\kappa=0.5$  (dimensionless) the Poisson ratio,  $h$  (cm) the wall thickness, and  $A_0 = \pi r_0^2$  (cm<sup>2</sup>) refers to the reference cross-sectional area<sup>8,54</sup> at  $p=0$ .

## 2.2.2 | Boundary conditions

The system of Equations (2) and (3) is hyperbolic with characteristics that propagate in opposite directions,<sup>56</sup> i.e., to be well-posed, each vessel needs an inlet and outlet boundary conditions. We enforce this by specifying the flow at the network inlet (Figure 3) and conservation of flow and continuity of pressure<sup>57</sup> at each junction, given by

$$p_p(L, t) = p_{d_i}(0, t) \quad \text{and} \quad q_p(L, t) = \sum_i q_i(0, t), \quad (4)$$

where the subscripts  $p$  and  $d_i$  ( $i=1,2$ ) refer to the parent and daughter vessels, respectively. Outlet boundary conditions for each terminal vessel are described by three-element Windkessel models (a resistor-capacitor-resistor (RCR) circuit) relating peripheral pressure  $p(L,t)$  and flow  $q(L,t)$  as

$$\frac{dp(L, t)}{dt} - R_p \frac{dq(L, t)}{dt} = q(L, t) \left( \frac{R_p + R_d}{R_d C} \right) - \frac{p(L, t)}{R_d C}, \quad (5)$$

where  $R_T=R_p+R_d$  (mmHg s/ml) is the total peripheral resistance,  $R_p$  is the proximal resistance,  $R_d$  is the distal resistance, and  $C$  (ml/mmHg) is the total compliance of the vascular region perfused by the terminal vessel (see Figure 3). The system of Equations 2 to 5 are solved numerically in C++ using the two-step Lax-Wendroff method, described in detail in Olufsen et al.<sup>8</sup>

## 2.2.3 | Nominal parameter values

The 1-D model has three types of parameters, shown in Table 2, specifying the network geometry, the fluid and vascular properties, and the inlet and outlet boundary conditions. Some of these can be measured or found in literature, while others must be inferred. Here, we describe how to compute nominal parameter values before performing model reduction and parameter inference using frequentist and Bayesian techniques.

**TABLE 2** List of parameter values and how they are calculated

Parameter	Units	Control Value	Hypoxic Value	Reference
$r_0$	[cm]	<sup>a</sup>	<sup>a</sup>	Qureshi, Colebank, Paun et al <sup>17</sup>
$L$	[cm]	<sup>a</sup>	<sup>a</sup>	Qureshi, Colebank, Paun et al <sup>17</sup>
$\rho$	[g/ml]	1.057	1.057	Riches et al <sup>58</sup>
$\nu$	[cm <sup>2</sup> /s]	0.0462	0.0462	Windberger et al <sup>59</sup>
$\delta$	[cm]	0.03	0.03	van de Vosse and Stergiopoulos <sup>3</sup>
$\kappa$	Dimensionless	0.5	0.5	Qureshi, Colebank, Paun et al <sup>17</sup>
$Z_c$	[mmHg s/ml]	26.0	150.6	Qureshi, Colebank, Schreier et al <sup>60</sup>
$T$	[s]	0.11	0.11	Qureshi, Colebank, Paun et al <sup>17</sup>
$\tau$	[s]	0.14	0.09	Qureshi, Colebank, Paun et al <sup>17</sup>
$R_T$	[mmHg s/ml]	Equation 8	Equation 8	Qureshi, Colebank, Paun et al <sup>17</sup>
$C$	[ml/mmHg]	Equation 8	Equation 8	Qureshi, Colebank, Paun et al <sup>17</sup>
$\beta = Eh/r_0$	[mmHg]	<sup>b</sup>	<sup>b</sup>	-
$r_p$	Dimensionless	<sup>b</sup>	<sup>b</sup>	-
$r_d$	Dimensionless	<sup>b</sup>	<sup>b</sup>	-
$c$	Dimensionless	<sup>b</sup>	<sup>b</sup>	-

<sup>a</sup>Parameters based on imaging data.

<sup>b</sup>Parameters inferred.

### Network geometry

Vessel length, radius, and connectivity are extracted from imaging data as described in Section 2.1. While these quantities carry uncertainty, we assume that all geometric properties are constant and known. The dimensions and connectivity of the different models are given in Table 1.

### Fluid and vascular properties

The blood density  $\rho=1.057$  (g/ml),<sup>58</sup> the kinematic viscosity  $\nu=0.0462$  (cm<sup>2</sup>/s), measured at a shear rate of 94 (s<sup>-1</sup>),<sup>59</sup> and the boundary layer thickness  $\delta \approx \sqrt{\nu T / 2\pi^3}$  are assumed constant. Here,  $T$  (s) denotes the length of the cardiac cycle, which is 0.112 and 0.107 (s) for the control mouse and hypoxic mouse, respectively. This difference is statistically insignificant<sup>17</sup> and has a negligible effect on model predictions, hence  $T=0.11$  for all simulations. The nominal value for the wall stiffness in the MPA ( $\beta_{MPA}$ ) is approximated as

$$\beta_{MPA} = \frac{2(A_0 Z_c)^2}{\rho}, \quad (6)$$

where the characteristic impedance  $Z_c$  is estimated from the slope of the pressure-flow loop including 95% of the flow during ejection phase.<sup>60</sup>

### Inflow and outlet conditions

We specify a control and hypoxic flow waveform at the inlet of the MPA, repeated for each cardiac cycle ( $T=1/\text{HR}$  (s)), for each mouse. At the outlet of each terminal vessel, we specify a three-element Windkessel model (Equation 5). This model has three parameters, two resistors, and a capacitor, given by  $\theta_{wk}=\{R_p, R_d, C\}$ . For each terminal vessel, the total peripheral resistance is  $R_T = R_p + R_d = \bar{p}/\bar{q}$ , where  $\bar{p}$  and  $\bar{q}$  denote the mean pressure and flow over the cardiac cycle (obtained from the data). Similar to previous studies,<sup>7,18</sup> we assume that the nominal proximal resistance is  $R_p=0.2R_T$  and that the distal resistance is  $R_d=R_T-R_p$ . As suggested by Stergiopoulos et al,<sup>10</sup> the peripheral compliance is calculated as  $C=\tau/R_T$ , where the time-constant  $\tau$  is estimated by fitting the diastolic pressure decay  $p_d(t)$  to an exponential function<sup>17,60</sup>

$$p_d(t) = p(t_d) \exp(-(t - t_d)/\tau), \quad (7)$$

where  $t_d$  denotes the onset of diastole.

For models with more than one vessel (i.e., the SB and FN models),  $\theta_{wk}$  are estimated by distributing  $R_T$  to each terminal vessel  $j$  as

$$R_{Tj} = \frac{\bar{p}}{\bar{q}_j}, \quad \text{and} \quad C_j = \frac{\tau}{R_{Tj}}, \quad (8)$$

where  $\bar{q}_j$  is the mean flow to vessel  $j$ , determined by applying Poiseuille's law recursively at each junction. This relation gives

$$\bar{q}_{d_i} = \frac{F_{d_i}}{\sum_i F_{d_i}} \bar{q}_p, \quad \text{where} \quad F_{d_i} = \left( \frac{\pi r_0^4}{8\mu L} \right)_{d_i} \quad \text{for } i = 1, 2. \quad (9)$$

Here  $\bar{q}_{d_i}$  and  $\bar{q}_p$  denote the mean flow in the daughter vessel  $i$  and parent vessel  $p$ , respectively. Similar to the SV model, the total resistance is distributed as  $R_{pj}=0.2R_{Tj}$  and  $R_{dj}=R_{Tj}-R_{pj}$ . Each outlet  $j$  requires specification of three parameters ( $R_{pj}, R_{dj}, C_j$ ), i.e., the SV model has three outlet parameters, the SB model has six outlet parameters, and the FN model has 33 outlet parameters.

## 2.3 | Parameter reduction

Assuming that the network geometry is fixed, the model parameters can be grouped into two categories: parameters in the 1-D model equations,  $\theta_{1D}^i = \{T, \nu, \rho, \delta, \beta_i\}$  for  $i=1, \dots, N_{ves}$ , where  $N_{ves}$  is the number of vessels and parameters needed to specify the outlet boundary conditions,  $\theta_{wk}^j = \{R_{pj}, R_{dj}, C_j\}$  for  $j=1, \dots, N_{term}$ , where  $N_{term}$  is the number of terminal vessels. The models studied here have 8, 13, and 58 parameters for the SV, SB, and FN models, respectively, yet data is only available in the MPA. The lack of downstream data makes parameter inference naturally ill-posed, as multiple parameters are to be inferred using one time-series signal. To address this problem, we introduce global scaling factors to reduce the number of inferred parameters.

For this study, we assume that the cardiac cycle length  $T$ , the kinematic viscosity  $\nu$ , the density  $\rho$ , and the boundary layer thickness  $\delta$  are constant. We assume the stiffness  $\beta$  is the same for each vessel in the control and hypoxic mice, as the proximal vessels have the same material properties.<sup>14,17,61</sup> As a result, only the Windkessel parameters  $R_p, R_d$ , and  $C$  are vessel-specific. From circuit theory, it is known that resistors and capacitors in parallel and series can be combined to compute the total resistance and capacitance for a circuit. The presence of multiple resistors and capacitors, which could be combined, leads to identifiability issues, i.e., inferred parameters may not be unique.<sup>23,62-64</sup> To avoid this, we simplify the parameter inference problem by introducing global scaling factors<sup>17,44</sup>  $r_p, r_d$ , and  $c$  for the Windkessel parameters at each terminal vessel  $j$

$$\tilde{R}_{pj} = r_p R_{pj}, \quad \tilde{R}_{dj} = r_d R_{dj}, \quad \tilde{C}_j = c C_j, \quad (10)$$

where  $(\cdot)$  refer to the scaled Windkessel parameters.

In summary, we fix parameters  $\{T, \nu, \rho, \delta\}$  as well as the nominal Windkessel parameters  $\{R_{pj}, R_{dj}, C_j\}$  for each terminal vessel  $j$ , leaving the reduced parameter set  $\theta=\{\beta, r_p, r_d, c\}$  to be inferred.

## 2.4 | Parameter inference

Inferred parameters  $\hat{\theta} = \{\hat{\beta}, \hat{r}_p, \hat{r}_d, \hat{c}\}$  are computed by minimizing

$$J(\theta) = \left( \frac{1}{N} \chi(t; \theta)^T \chi(t; \theta) \right), \quad \chi(t; \theta) = \begin{bmatrix} p_m(L/2, t_1) - p_{data}(t_1) \\ \vdots \\ p_m(L/2, t_N) - p_{data}(t_N) \end{bmatrix}, \quad (11)$$

where  $N$  is the number of data points,  $p_{data}(t_i)$  is the MPA pressure data measured at  $t=t_i$ , and  $p(L/2, t_i)$  is the corresponding model prediction at the midpoint of the MPA for a given value of  $\theta$ . Throughout this paper, we use  $(\cdot)$  to denote quantities that are inferred using either the frequentist or Bayesian techniques described in Section 3. Moreover, the

scaling factors shown in Equation 10 always adjust the nominal parameter estimates  $R_{pj}$ ,  $R_{dj}$ , and  $C_j$ , which are calculated using Equations 8 and 9.

### 3 | MODEL ANALYSIS

To determine the influence of model parameters on the MPA pressure, we use local and global sensitivity methods. We analyze parameter correlations and pairwise parameter distributions to determine a subset of parameters that can be inferred given the model and available data. We use both frequentist and Bayesian inference methods to infer point-estimates and posterior parameter distributions by minimizing the least squares error between model predictions and MPA pressure measurements. Subsequently, we use forward uncertainty propagation to quantify the uncertainty of model predictions in the MPA and downstream vasculature.

#### 3.1 | Sensitivity analysis

Sensitivity analysis characterizes the influence of parameters on the model output. This type of analysis provides insight into future data collection methods and experimental designs, as parameters that are more influential should be prioritized for experimental measurement.<sup>65</sup> Conversely, a lack of agreement between sensitivity analysis and physiological knowledge can imply missing model physics or a need for different measurements. In this study, we use derivative-based local sensitivity analysis<sup>20</sup> and Morris screening<sup>66</sup> (global) to quantify the parameter influence on MPA pressure predictions: the quantity of interest. Local sensitivity analysis is computationally efficient and informative if reasonable nominal parameter values are known and the model is not too nonlinear, whereas global sensitivity analysis provides a more robust analysis of the model at a much higher computational cost. Since MPA pressure varies in time, we compute both the averaged and time-varying model sensitivities.

##### 3.1.1 | Local sensitivity analysis

Derivative-based sensitivity analysis computes the model sensitivity with respect to a single parameter at a fixed value.<sup>24,64,67</sup> For a given quantity of interest  $f(t; \theta)$ , the sensitivity  $S_i(t_j; \theta)$  is defined as

$$S_i(t_j; \theta) = \frac{\partial f(t_j; \theta)}{\partial \theta_i}, \quad i = 1, 2, \dots, P, \quad j = 1, 2, \dots, N, \quad (12)$$

where  $\theta_i$  denotes the parameter of interest,  $P$  is the number of parameters in the model,  $t_j$  is the  $j$ th time point, and  $N$  is the number of time steps in the model output. The sensitivity matrix  $S(t; \theta)$  is constructed by appending all the  $N \times 1$  sensitivity vectors  $S_i(t; \theta)$ . In this study, we approximate the model sensitivity using the centered finite difference method

$$\frac{\partial f}{\partial \theta_i} \approx \frac{f(t; \theta + \mathbf{e}_i \psi) - f(t; \theta - \mathbf{e}_i \psi)}{2\psi}, \quad (13)$$

where  $\psi$  is the step size and  $\mathbf{e}_i$  is a unit vector in the  $i$ th direction. Finite difference methods for sensitivity equations are limited by the accuracy of the numerical solver for the given system of equations,<sup>28</sup> but are more computationally efficient.<sup>20,24,29,30</sup> We choose a relatively larger number of time steps per period (8192) to ensure numerical stability and satisfaction of the Courant-Fredrich-Lowy (CFL) condition in every vessel, making  $\psi = \sqrt{\Delta t} \approx 10^{-3}$  for the second-order accurate Lax-Wendroff scheme.

To make sensitivities of similar magnitude and prevent negative parameter values, we log scale the parameters,  $\tilde{\theta} = \log(\theta)$ . The resulting log-scaled sensitivities are given by

$$\tilde{S}_i(t; \theta) = \frac{\partial f(t; \theta)}{\partial \tilde{\theta}_i} = \frac{\partial f(t; \theta)}{\partial \theta_i} \theta_i, \quad i = 1, 2, \dots, P. \quad (14)$$

Local sensitivities are computed as functions of time over one cardiac cycle, and ranked sensitivities  $\bar{S}_i$  are computed by averaging sensitivities over one cardiac cycle using the 2-norm

$$\bar{S}_i = \|\tilde{S}_i\|_2. \quad (15)$$

It should be noted that sensitivity computations are done over one cardiac cycle after the system has reached steady, oscillatory behavior, i.e., when transient effects have dissipated.

### 3.1.2 | Global sensitivity analysis

We use Morris screening<sup>21</sup> to compute global sensitivity metrics, which is of similar accuracy as Sobol' based total sensitivities computed using variance-based methods.<sup>31,32</sup> Morris screening involves the computation of “elementary effects,” which determine the relative change of the model output to a relative change in parameter values. The screening method quantifies the effects of a parameter  $\theta_i$  on the output quantity as (a) negligible overall, (b) linear and additive, or (c) having nonlinear effects or higher order interactions with other parameters. To perform this analysis, parameters are mapped from their bounded parameter space  $\Theta \in \mathbb{R}^P$  to the unit hypercube  $[0,1]^P$ , where  $P$  denotes number of parameters analyzed. Using a uniform, bounded prior distribution restricts the model analysis to a physiologically relevant parameter subspace without invoking a bias. The elementary effects are computed as

$$d_i(t; \theta) = \frac{f(t; \theta + e_i \Delta) - f(t; \theta)}{\Delta}. \quad (16)$$

The step size  $\Delta$  is chosen from the set  $\Delta \in \{1/(\mathcal{M} - 1), 2/(\mathcal{M} - 1) \dots, (\mathcal{M} - 2)/(\mathcal{M} - 1)\}$ , where  $\mathcal{M}$  denotes the number of parameter perturbation levels used in the screening method, i.e., the number of possible perturbation sizes. To preserve symmetry of the parameter distributions, we choose  $\mathcal{M}$  to be even.<sup>21,23,31</sup> The elementary effects are then computed by sampling  $K$  values from a uniform distribution for the parameter  $\theta_i^j, j=1, 2, \dots, K$ . To compare elementary effects at different points in the parameter space, we compute 2-norm elementary effects, denoted by  $\tilde{d}_i^j(\theta) = \|d_i^j(t; \theta)\|_2$ . We employ the algorithm by Wenthworth et al<sup>32</sup> scaling the step size  $\Delta$  by the parameter magnitude.

The elementary effects' mean and variance are obtained by integrating the outcomes from multiple iterations. The modified Morris indices are calculated as

$$\mu_i^* = \frac{1}{K} \sum_{j=1}^K |\tilde{d}_i^j|, \quad \sigma_i^2 = \frac{1}{K-1} \sum_{j=1}^K (\tilde{d}_i^j - \mu_i^*)^2, \quad (17)$$

where  $\mu^*$  quantifies the individual effect of the input on the output, i.e., the sensitivity of the model with respect to the parameter selected, while the variance estimate  $\sigma^2$  describes the variability in the model sensitivity due to parameter interactions or nonlinearity. Parameters with a large  $\mu^*$  and  $\sigma^2$  have large effects on the model output and are highly nonlinear in the model. Similar inference can be made for other combinations of  $\mu^*$  and  $\sigma^2$ . Following the work by Wenthworth et al,<sup>32</sup> we compute the metric  $\sqrt{\mu^{*2} + \sigma^2}$  to rank the parameters, which takes into account the magnitude and variability of the elementary effects.

For the randomized Morris algorithm, we set the number of samples  $K=50$ , the number of levels of the parameter space  $\mathcal{M} = 20$ , and the step size  $\Delta = \frac{\mathcal{M}}{2(\mathcal{M} - 1)} \approx 0.526$ . The parameter bounds are  $\beta_{control} \in [7.5, 75]$  and  $\beta_{hypoxic} \in [75, 750]$  mmHg for the control and hypoxic mice and  $0.05 \leq r_p, r_d, c \leq 3$  for both the control and hypoxic animals. These bounds ensure that model predictions are within the physiological range for both the control and hypoxic mouse without invoking a strong bias in the prior parameter distributions.

### 3.2 | Correlation analysis

To identify pairwise parameter correlations and find a reduced parameter subset, we analyze the covariance matrix  $V$ , which for a constant observation variance  $s^2$  can be approximated asymptotically<sup>68</sup> as

$$V = s^2 \left[ \tilde{S}(t; \theta)^T \tilde{S}(t; \theta) \right]^{-1}, \quad s^2 = \frac{1}{N - P} \left[ \chi(t; \theta)^T \chi(t; \theta) \right], \quad (18)$$

where  $\chi(t;\theta)$  is the residual defined in Equation 11,  $\tilde{S}$  is the sensitivity matrix defined in Equation 12, and  $P$  is the number of parameters. We calculate correlations as

$$\nu_{ij} = \frac{V_{ij}}{\sqrt{V_{ii} V_{jj}}}, \quad (19)$$

where  $\nu_{ij}$  is a symmetric matrix with diagonal elements  $\nu_{ii}=1$  and  $|\nu_{ij}| \leq 1$ . High pairwise parameter correlations can cause optimization routines to fail in finding a unique (local) minimum.<sup>23,43,67</sup> Parameters are only correlated if  $\nu_{ij}=1$ .<sup>23</sup> Yet, previous studies have used cutoff values ranging from 0.8 to 0.95.<sup>23,24,45,46,69</sup> In this study, we use this guideline when determining correlations.

### 3.3 | Optimization

Identifiable model parameters are inferred using a sequential quadratic programming (SQP) algorithm, minimizing Equation 11 within specified parameter bounds.<sup>44</sup> The complexity of the 1-D fluids model introduces a need for parameter bounds, ensuring that the numerical solver converges without violating the CFL condition. The physiological interpretation of parameter values also provide bounds, which may be more restrictive than the numerical bounds.

The SQP algorithm is executed via the MATLAB function `fmincon` with the `sqp` option. For the control mouse, the parameter bounds were set at  $\beta \in [7.5, 75]$  mmHg and  $0.05 \leq r_p, r_d, c \leq 3$ , and for the hypoxic mouse, we set  $\beta \in [75, 750]$  mmHg and  $0.05 \leq r_p, r_d, c \leq 3$ . For each optimization, eight initial values are sampled from a uniform distribution spanning the intervals given above. Using eight initial conditions showed that the optimization converged to a global minimum within the parameter bounds. Optimization was conducted on an iMac (3.4 GHz Intel Core i7, 16GB RAM, OS 10.13.4). The algorithm is iterated until the least squares minimization problem has converged, i.e.,  $|J_N - J_{N-1}| < 10^{-8}$ .

### 3.4 | Uncertainty quantification

Given the limited data available from PH patients, it is important to understand how uncertainties in model parameters propagate to model predictions. We use frequentist and Bayesian methods to propagate uncertainty predictions through each model. Frequentist methods treat parameters as fixed and unknown, encouraging traditional optimization-based parameter inference and model confidence intervals as discussed in Smith.<sup>23</sup> In contrast, the Bayesian framework treats parameters as random variables and incorporates a priori knowledge, via prior parameter distributions, and a likelihood function to construct posterior distributions that best explain the observed data. Sampling from the posterior distributions can then propagate uncertainties forward and construct model confidence and credible intervals. Bayesian methods provide detailed uncertainty but are more computationally expensive than frequentist methods. On the other hand, frequentist parameter inference can fail if parameters are nonidentifiable or highly correlated, while the Bayesian methods can expose these relationships and still provide information about parameter uncertainty. Below, we describe both methods, highlighting the advantages and disadvantages for each.

#### 3.4.1 | Frequentist analysis

In the frequentist framework, confidence and prediction intervals are constructed for both the parameters and the model predictions where data is available. To compute the confidence intervals for a given parameter, we consider inferred parameters  $\hat{\theta}$  that minimize the cost function  $J$  defined in Equation 11 and the associated local sensitivity matrix  $\hat{S} = \tilde{S}(t; \hat{\theta})$ . Using this framework and the constant, estimated observation variance  $\hat{s}^2$  from Equation 18, the parameter confidence intervals are calculated as

$$\theta_i^{CI} \equiv \left[ \hat{\theta}_i - t_{N-P}^{1-\alpha/2} \hat{s} \sqrt{\left( \hat{S}^T \hat{S} \right)^{-1}}, \hat{\theta}_i + t_{N-P}^{1-\alpha/2} \hat{s} \sqrt{\left( \hat{S}^T \hat{S} \right)^{-1}} \right], \quad (20)$$

where  $t_{N-P}^{1-\alpha/2}$  denotes a  $t$  statistic with  $N-P$  degrees of freedom and a  $1-\alpha=0.95$  confidence level. The confidence interval for the model response,  $y^{CI}(t)$ , can be computed in a similar fashion

$$y^{CI}(t_i) \equiv \left[ y(t_i; \hat{\theta}) - t_{N-P}^{1-\alpha/2} \hat{s} \sqrt{\Gamma_i}, y(t_i; \hat{\theta}) + t_{N-P}^{1-\alpha/2} \hat{s} \sqrt{\Gamma_i} \right], \quad (21)$$

where  $\Gamma_i = G_i^T (\hat{S}^T \hat{S})^{-1} G_i$  and

$$G_i^T = \left( \frac{y(t_i; \hat{\theta})}{\tilde{\theta}_1}, \dots, \frac{y(t_i; \hat{\theta})}{\tilde{\theta}_P} \right).$$

Lastly, the prediction intervals for the model response are calculated as

$$y^{PI}(t_i) \equiv \left[ y(t_i; \hat{\theta}) - t_{N-P}^{1-\alpha/2} \hat{s} \sqrt{1 + \Gamma_i}, y(t_i; \hat{\theta}) + t_{N-P}^{1-\alpha/2} \hat{s} \sqrt{1 + \Gamma_i} \right]. \quad (22)$$

It should be noted that since data is only collected at the inlet of the MPA, we cannot estimate the variance  $\hat{s}^2$  that would be needed to construct accurate confidence and prediction intervals in other vessels of the network.

### 3.4.2 | Bayesian analysis

In contrast to the frequentist framework, Bayesian credible and prediction intervals are computed from the posterior distributions of the parameters in question. In this study, we employ the DRAM algorithm<sup>44,70,71</sup> to determine posterior parameter distributions and study pairwise parameter correlations (see Appendix A for more details on the algorithm).

The parameter posterior,  $\pi(\theta|y)$  is computed using Bayes' formula

$$\pi(\theta|y) = \frac{\pi(y|\theta)\pi_0(\theta)}{\pi(y)} = \frac{\pi(y|\theta)\pi_0(\theta)}{\int_{\mathbb{R}^P} \pi(y|\theta)\pi_0(\theta)d\theta} \quad (23)$$

for the data  $y$ , where  $\pi(y|\theta)$  is the likelihood function,  $\pi_0(\theta)$  is the prior distribution, and  $\int_{\mathbb{R}^P} \pi(y|\theta)\pi_0(\theta)d\theta$  is a normalization factor. We assume that the prior distribution  $\pi_0(\theta)$  is flat (i.e., uniformly distributed) over the physiological bounds, and that the likelihood function  $\pi(y|\theta)$  in Equation 23 can be specified and reflects statistical properties of the data. We assume that the measurement errors,  $\epsilon_i$ , are independent and identically distributed (iid), normally distributed random variables with mean zero and constant variance  $\sigma_\epsilon^2$ , i.e.,  $\epsilon_i \sim \mathcal{N}(0, \sigma_\epsilon^2)$ . Under these assumptions, the likelihood function is given as

$$\mathcal{L}(\theta, \sigma_\epsilon^2|y) = \pi(y|\theta) = \frac{1}{(2\pi\sigma_\epsilon^2)^{N/2}} e^{-\chi^T \chi / 2\sigma_\epsilon^2}, \quad (24)$$

where  $\chi$  is the residual defined in Equation 11.

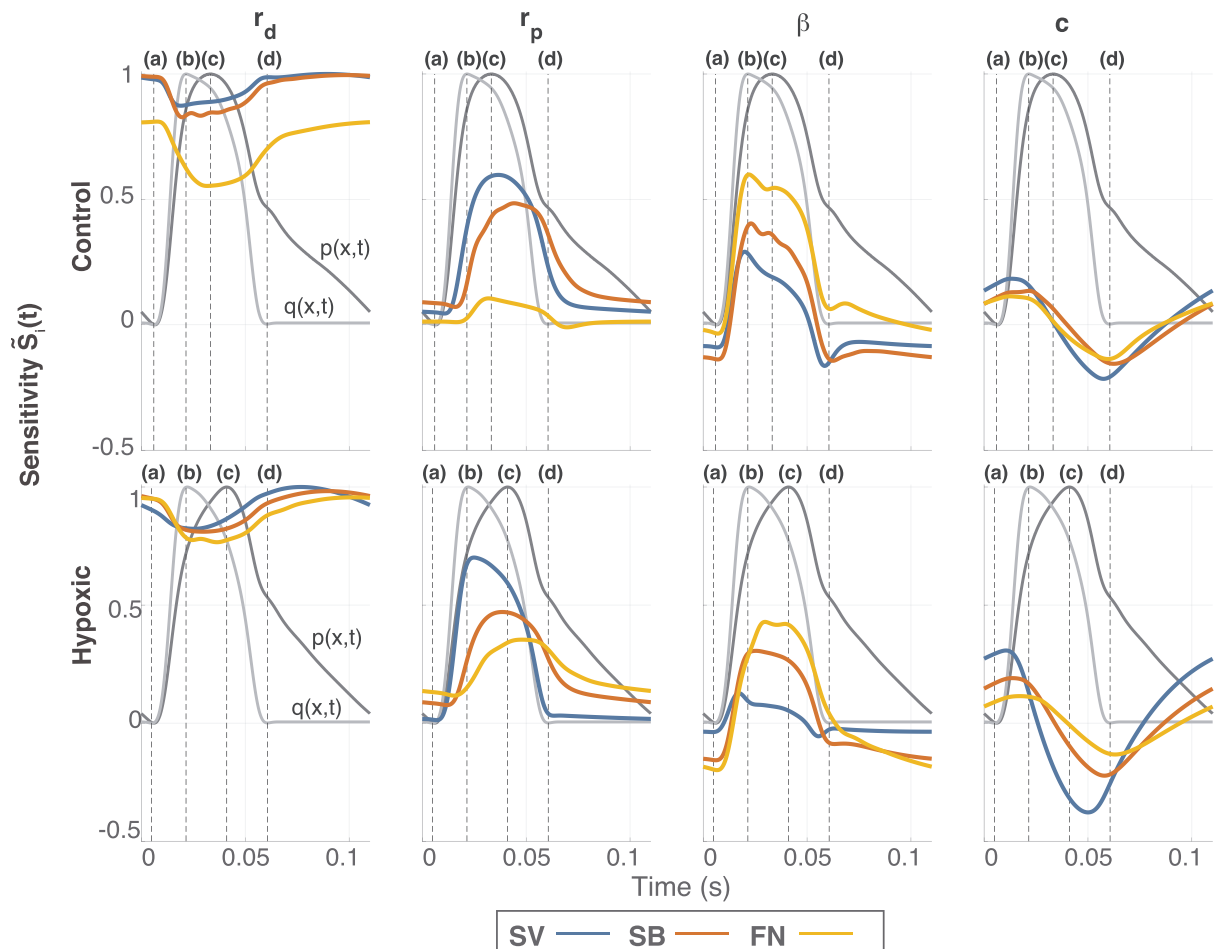
For MCMC methods, convergence to the true posterior distribution is only guaranteed for an infinite number of samples, i.e.,  $M \rightarrow \infty$ . In practice, the number of samples should be large enough to ensure that the chains have visibly converged. In this study, we use the Geweke test,<sup>72</sup> which determines convergence of a MCMC chain by comparing the first 10% and last 50% of the chain for significant differences in the mean and computes a p-value from a Z-statistic. p-values close to zero indicate that the null hypothesis of equal means between the two chains should be rejected, suggesting non-convergence.

Subsequently, the posterior distribution  $\pi(\theta|y)$  is used to compute credible and prediction intervals for the model response. To do so, we draw 2000 samples from the posterior distribution propagating uncertainties forward through the model computing both credible and prediction intervals for the pressure in the MPA.<sup>23,70</sup>

## 4 | RESULTS

### 4.1 | Sensitivity analysis

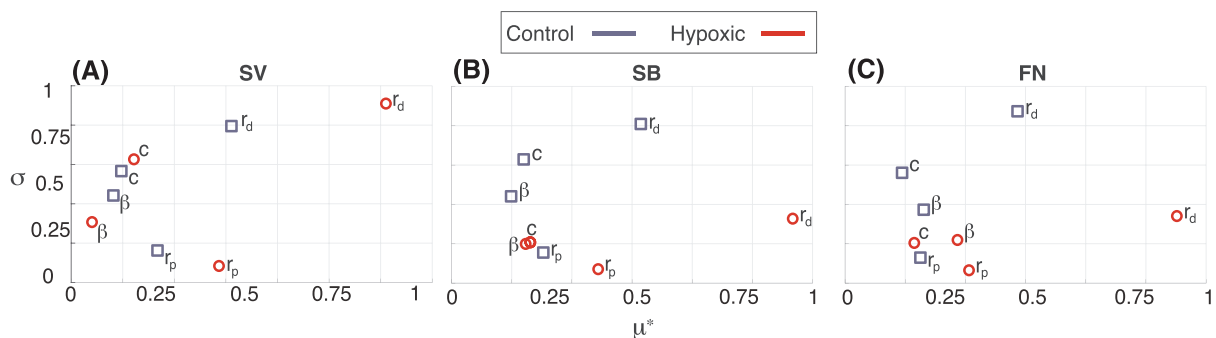
Figure 4 shows the sensitivity of MPA pressure predictions to the four parameters in the control and hypoxic mouse. Normalized pressure and flow waveforms are plotted in the background to help identify which sections of the cardiac cycle (systole from (b)-(d), diastole from (a)-(b) and (d)-(a)) are most sensitive to these parameters. Results show that the distal vascular resistance has the largest influence on pressure predictions for all networks in both mice, being most influential during periods of diastole. Analysis of the remaining parameters show that the vessel stiffness  $\beta$  becomes more influential as more branches are added, while the proximal resistance  $r_p$  scaling factor becomes less influential, indicating that model sensitivity to the proximal resistances  $R_p$  is reduced. We note that the magnitude of model sensitivity to compliance does not change significantly as more vessels are added to the network but does show a slight decrease in influence in the hypoxic mouse when the network size increases. The time-varying sensitivities reveal that both proximal resistance ( $r_p$ ) and large artery stiffness ( $\beta$ ) have a greater effect on MPA pressure during systole. However,  $r_p$  becomes less influential on MPA pressure than  $\beta$  once more vessels are added to the network. It is worth noting that the model sensitivity to compliance oscillates, having a largest relative influence on model predictions at the start and end of systole (from (b)-(c) and (d)-(a)). Figure 4 also shows that time-varying model sensitivities maintain a similar shape for each parameter but slightly shift forward or backward in time as more vessels are added.



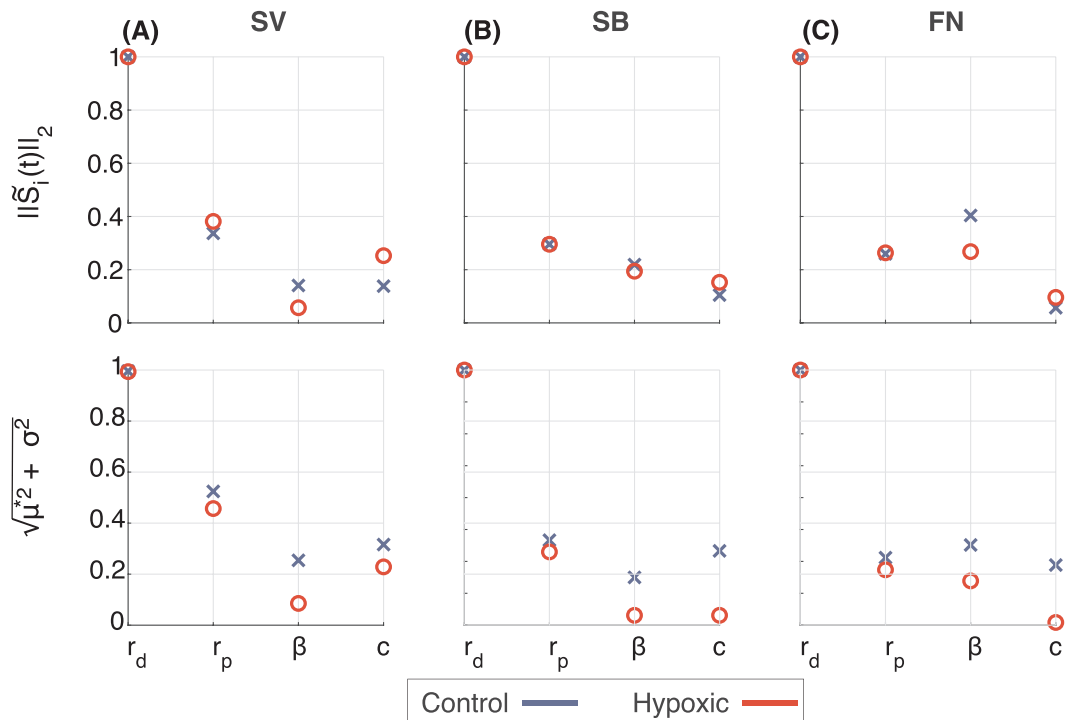
**FIGURE 4** Normalized local sensitivities in the root of the main pulmonary artery (MPA), pressure during the cardiac cycle for the single vessel (SV) (blue), single bifurcation (SB) (red), and full network (FN) (yellow) models. Light and dark gray lines denote the normalized flow and pressure predictions, respectively. Dashed vertical lines indicate (a) the start of systole, (b) the time of maximum flow, (c) the time of maximum pressure, and (d) the start of diastole. Results show that  $r_d$  is the most influential parameter regardless of model or disease type and that vessel stiffness  $\beta$  increases in influence as more vessels are added to the system

Figure 5 shows the scaled mean and standard deviation of the elementary effects from the global sensitivity analysis. These results agree with the local analysis, showing that the distal resistance is most influential (characterized by  $\mu^*$ ) and that  $r_d$  has the largest variability in influence (characterized by  $\sigma$ ) regardless of the network size or disease. The variability of influence for the compliance parameter in the control mouse is consistently larger than the average influence, yet the hypoxic mouse has a decrease in compliance variability when moving to the larger networks. Overall, the results show that distal resistance in the network has the largest interaction and/or nonlinear effect while proximal resistance has the smallest variability in influence.

In summary, both the local and global analysis show that the large artery stiffness  $\beta$  becomes more influential as more vessels are added to the network, depicted in Figure 6. The local method shows a decrease in the effects of compliance, yet the global methods reveal a high variance in the influence of compliance on MPA pressure predictions, thus ranking it higher for the control mouse. These results indicate that the influence of compliance on MPA pressure is



**FIGURE 5** Normalized Morris indices  $\mu^*$  and  $\sigma$  for the (A) single vessel (SV), (B) single bifurcation (SB), and (C) full network (FN) models in the control (blue squares) and hypoxic (red circles) mice. For both mice,  $r_d$  has the largest value of  $\mu^*$  and  $\sigma$ . The global sensitivities show that the parameter  $\beta$  increases in influence as more vessels are added to the network



**FIGURE 6** Ranking of parameters in the (A) single vessel (SV), (B) single bifurcation (SB), and (C) full network (FN) models based on their local and global sensitivity results. All ranking metrics were scaled to the rank value of  $r_d$ , which was largest in magnitude. Blue x's indicate control models while red circles indicate hypoxic models

highly dependent on the parameter space for  $\beta$ ,  $r_p$ , and  $r_d$ . Aside from the compliance scaling factor  $c$ , the parameter rankings are similar for the local and global methods.

## 4.2 | Correlation analysis

The local parameter sensitivities are used to compute the covariance (Equation 18) and correlation matrices for each model. For both animals, the largest correlation is found in the FN network between  $r_p$  and  $\beta$ . For the control mouse, the correlation coefficient  $v_{r_p\beta} = -0.84$ , and for the hypoxic mouse,  $v_{r_p\beta} = -0.92$ . To study this correlation over a larger parameter space, we conducted a DRAM simulation on each model for both mice and plotted pairwise parameter posterior distributions. Results for the FN model shown in Figure 7 agree with the local covariance analysis. For the hypoxic mouse, the correlation coefficient  $v_{r_p\beta} = -0.97$ , and for the control mouse  $v_{r_p\beta} = -0.89$ . To remove the correlation, we fixed  $\beta$  at its nominal value and repeated the DRAM simulations, shown in Figure 7B, which reduced parameter correlations  $v_{ij} < 0.8$ . Moreover, inferring both  $r_p$  and  $\beta$  resulted in significant differences in  $\beta$  between networks, which within an animal should have the same material properties. Therefore, to enforce that proximal vessels within a mouse have the same stiffness, we inferred a single stiffness over all three networks. It should be noted that  $\beta$  may still be correlated with  $r_p$ , but this approach resulted in inferred values consistent with our physiological hypothesis; as noted by Smith,<sup>23</sup> having correlations between parameters does not mean they cannot be inferred.

## 4.3 | Frequentist analysis

As noted in Section 4.2, we estimate a single  $\beta$  value and individual scaling factors for each network, i.e., we estimate a total of 10 parameters

$$\hat{\theta}_0 = \{\hat{\beta}, \hat{r}_p^{SV}, \hat{r}_d^{SV}, \hat{c}^{SV}, \hat{r}_p^{SB}, \hat{r}_d^{SB}, \hat{c}^{SB}, \hat{r}_p^{FN}, \hat{r}_d^{FN}, \hat{c}^{FN}\} = \{\hat{\beta}, \hat{\theta}^{SV}, \hat{\theta}^{SB}, \hat{\theta}^{FN}\}, \quad (25)$$

minimizing the least squares cost defined in Equation 11 for the control and hypoxic mouse.

To ensure convergence, we propagate eight initial values sampled from a uniform parameter distribution over the intervals given in Section 4.1. Nominal and optimal model predictions are depicted in Figure 8 (panels A,B and C,D respectively) and the optimal parameter values are given in Table 3. Results depicted in Figure 8 show that all models fit the data well after optimization, significantly improving the costs (in Table 4) from the nominal parameter fits. First, we note that all three models provide an equally good fit within disease type, as the least squares error is of the same order of magnitude for each network. However, simulations do reveal that the hypoxic models fit the data better than the control model, as the least squares error is an order of magnitude smaller,  $10^{-2}$  vs  $10^{-1}$ .

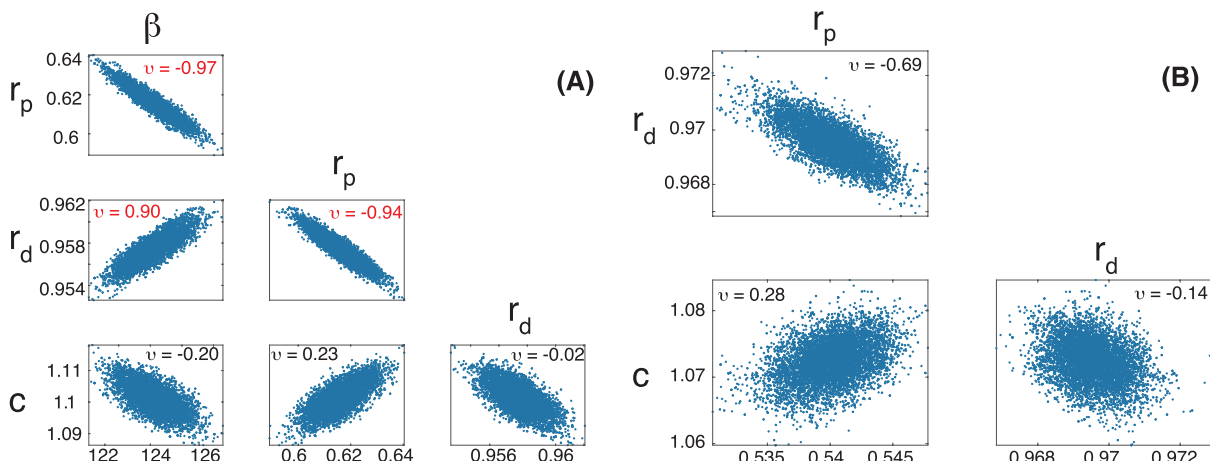


**FIGURE 7** (A) Pairwise plots from 10,000 iterations in Delayed Rejection Adaptive Metropolis (DRAM) for the hypoxic full network (FN) model using the full parameter set  $\theta = (\beta, r_p, r_d, c)$ ; (B) Pairwise plots from DRAM when  $\beta$  was fixed at its nominal value. (A) shows that the parameters  $\beta$  and  $r_p$  are highly correlated, as was indicated by the structured correlation results. By fixing  $\beta$  (panel B), the correlation between parameters, denoted by  $v$ , decreases

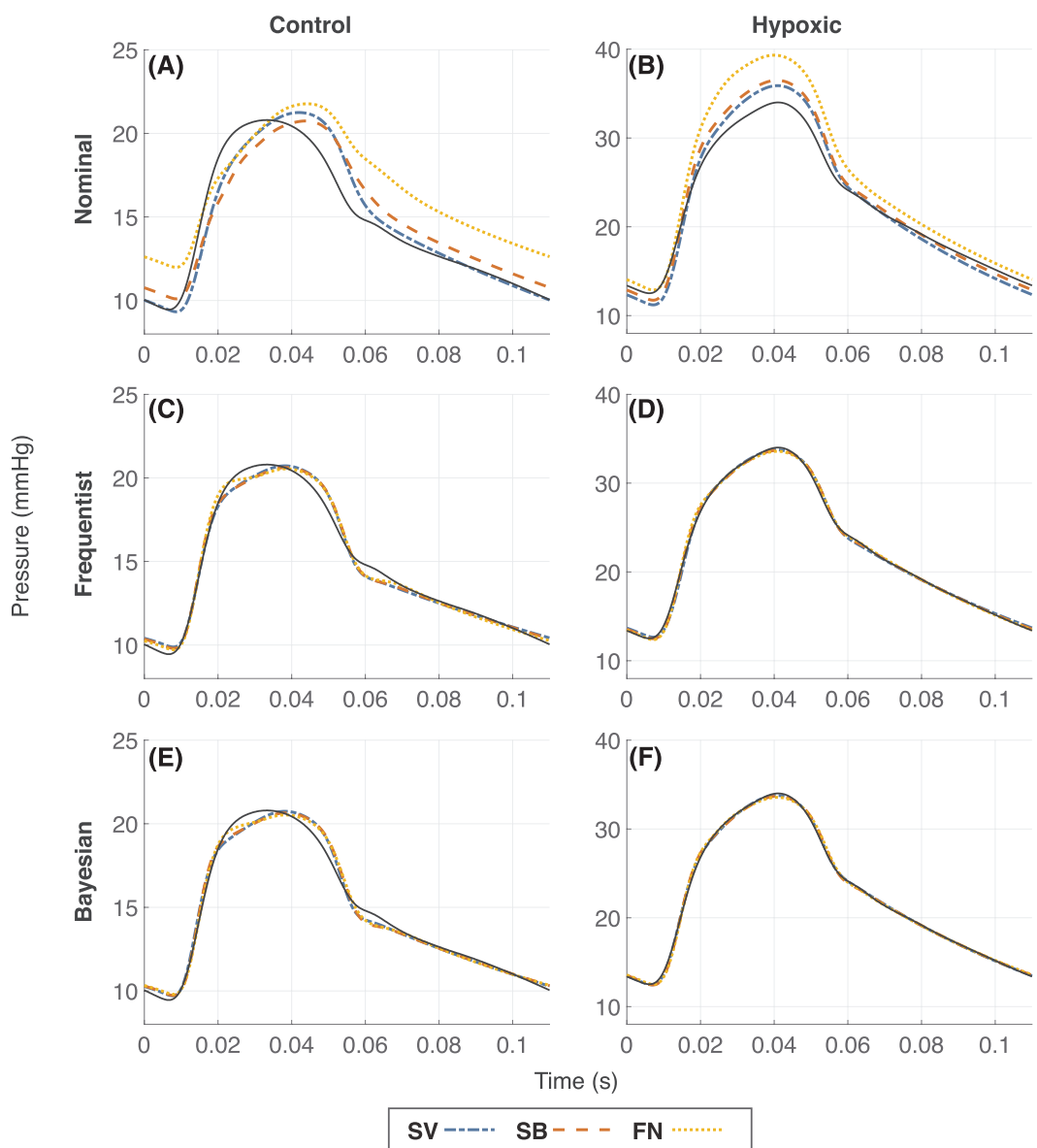


**FIGURE 8** The main pulmonary artery (MPA) pressure data (black, solid curve) and predictions with the single vessel (SV) (dash-dot, blue line), single bifurcation (SB) (dashed, red line), and full network (FN) (dotted, yellow line) models. MPA pressure waveforms for the control (left column) and hypoxic (right column) models are plotted using (A and B) the nominal parameters, (C and D) the optimized parameter values, and (E and F) the maximum a posteriori parameters

Table 3 reports inferred vessel stiffness  $\beta$ , optimal values for the scaling factors  $r_p, r_d$ , and  $c$ , the ratio of proximal to total resistance  $R_p/R_T$ , as well as the total peripheral resistance  $R_T^{WK}$  and the peripheral compliance  $C^{WK}$  for the whole network (calculated by summing the resistance and capacitance in parallel) for each network and each mouse pre and post optimization. The latter is done using the optimized scaling factors in Equation 10. The proximal to total resistance ratio decreases as the number of vessels in the network is increased for both the control and hypoxic mouse, but remains close to the nominal value of 0.2 for the smallest two networks. In contrast, the FN model shows a larger decrease in this ratio, indicating a larger relative value for  $R_d$ . The total resistance  $R_T^{WK}$  was consistently larger in the hypoxic mouse versus the control, whereas the compliance  $C^{WK}$  was higher for the control mouse, deviating little from our nominal estimates. The total peripheral resistance contributed from the Windkessel models decreased as the network size increased, whereas the total compliance increased. Frequentist parameter confidence intervals (Table 5) are calculated at the optimized values  $\hat{\theta}$  obtained from the SQP algorithms. Results show that the intervals for the control parameters are larger than those found for the hypoxic parameters, a result of the larger residual obtained with the control models. For the FN model, we calculated frequentist prediction intervals for MPA pressure using Equation 21 (compared with Bayesian results in Figure 10).

**TABLE 3** Nominal and optimized parameter values and the relative change to the nominal estimates after optimization

Model	Parameter	Control			Hypoxic		
		Nominal Estimate	Optimized Value	Relative Change (%)	Nominal Estimate	Optimized Value	Relative Change (%)
-	$\beta$	26.0	42.9	65	150.9	136.6	-10
SV	$r_p$	1	$8.84 \times 10^{-1}$	-12	1	$8.86 \times 10^{-1}$	-12
SV	$r_d$	1	1.02	2	1	1.02	2
SV	$c$	1	1.44	44	1	1.21	21
SV	$R_p/R_T$	0.2	0.18	-11	0.2	0.18	-11
SV	$R_T^{WK}$	78.4	77.6	-1	147	146	-0.7
SV	$C^{WK}$	$1.7 \times 10^{-3}$	$2.5 \times 10^{-3}$	44	$5.9 \times 10^{-4}$	$7.1 \times 10^{-4}$	21
SB	$r_p$	1	$8.00 \times 10^{-1}$	-20	1	$8.21 \times 10^{-1}$	-18
SB	$r_d$	1	$9.95 \times 10^{-1}$	-0.5	1	1.00	0.3
SB	$c$	1	1.34	34	1	1.14	14
SB	$R_p/R_T$	0.2	0.17	-17	0.2	0.17	-15
SB	$R_T^{WK}$	78.4	74.9	-4	147	142	-3
SB	$C^{WK}$	$1.7 \times 10^{-3}$	$2.3 \times 10^{-3}$	34	$5.9 \times 10^{-4}$	$6.7 \times 10^{-4}$	14
FN	$r_p$	1	$1.34 \times 10^{-1}$	-87	1	$5.40 \times 10^{-1}$	46
FN	$r_d$	1	$8.82 \times 10^{-1}$	-12	1	$9.70 \times 10^{-1}$	3
FN	$c$	1	1.62	62	1	1.07	7
FN	$R_p/R_T$	0.2	0.04	-82	0.2	0.12	-39
FN	$R_T^{WK}$	78.4	57.4	-27	147	130	-12
FN	$C^{WK}$	$1.7 \times 10^{-3}$	$2.8 \times 10^{-3}$	62	$5.9 \times 10^{-4}$	$6.3 \times 10^{-4}$	7

Note. The wall parameter  $\beta$  was the same for all three models in each mouse. Units:  $\beta$  (mmHg),  $R_T^{WK}$  (mmHg s/ml),  $C^{WK}$  (ml/mmHg), and  $r_p, r_d, c, R_p/R_T$  (dimensionless).

Abbreviations: FN, full network; SB, single bifurcation; SV, single vessel.

**TABLE 4** Least squares cost for all simulations using both frequentist and Bayesian methods

Model	Control		Hypoxic	
	$J_{opt}$	$J_{DRAM}$	$J_{opt}$	$J_{DRAM}$
SV	$1.71 \times 10^2$	$1.53 \times 10^2$	$6.08 \times 10^1$	$2.12 \times 10^1$
SB	$1.79 \times 10^2$	$1.76 \times 10^2$	$5.28 \times 10^1$	$5.16 \times 10^1$
FN	$1.44 \times 10^2$	$1.38 \times 10^2$	$7.97 \times 10^1$	$7.03 \times 10^1$

Abbreviations: FN, full network; SB, single bifurcation; SV, single vessel.

#### 4.4 | Bayesian analysis

DRAM simulations were initialized using the inferred parameters from the SQP optimization. The stiffness parameter was fixed at its optimal value  $\hat{\beta}$ , while the scaling parameters  $\{r_p, r_d, c\}$  were allowed to vary. Each simulation used a 2000 iteration burn-in period to initialize a 10 000 iteration chain, which allowed for convergence to the posterior distribution. We prescribed a uniform prior distribution spanning  $\pm 50\%$  of the optimized value for each parameter, facilitating adequate exploration of the parameter space. The posterior densities for all three models are shown in Figure 9, with initial point-estimates (the optimized values from the SQP optimization,  $\hat{\theta}$ ) marked with asterisks on the density curves. The Geweke test statistics for each DRAM chain had a  $P \geq .98$  for all models and both animals (control and hypoxic), suggesting convergence.

**TABLE 5** Frequentist confidence intervals for the optimized Windkessel parameters  $\hat{\theta} = \{r_p, r_d, c\}$  and Bayesian posterior variances for the control and hypoxic models

Model	Parameter	Optimized Value	Control			Hypoxic	
			Confidence Interval	Posterior $\sigma_{\theta}^2$	Optimized Value	Confidence Interval	Posterior $\sigma_{\theta}^2$
SV	$r_p$	$8.84 \times 10^{-1}$	$[8.76-8.93] \times 10^{-1}$	$7.93 \times 10^{-5}$	$8.85 \times 10^{-1}$	$[8.81-8.88] \times 10^{-1}$	$1.56 \times 10^{-5}$
SV	$r_d$	1.02	[1.01–1.02]	$1.25 \times 10^{-5}$	1.02	[1.02–1.02]	$2.54 \times 10^{-6}$
SV	$c$	1.44	[1.42–1.46]	$9.20 \times 10^{-4}$	1.21	[1.21–1.22]	$3.98 \times 10^{-5}$
SB	$r_p$	$7.96 \times 10^{-1}$	$[7.85-8.08] \times 10^{-1}$	$1.06 \times 10^{-4}$	$8.21 \times 10^{-1}$	$[8.17-8.24] \times 10^{-1}$	$1.53 \times 10^{-5}$
SB	$r_d$	$9.95 \times 10^{-1}$	$[9.92-9.98] \times 10^{-1}$	$1.45 \times 10^{-5}$	1.00	[1.00–1.00]	$1.57 \times 10^{-6}$
SB	$c$	1.34	[1.32–1.36]	$1.15 \times 10^{-3}$	1.14	[1.14–1.15]	$4.05 \times 10^{-5}$
FN	$r_p$	$1.35 \times 10^{-1}$	$[0.75-1.95] \times 10^{-1}$	$2.76 \times 10^{-4}$	$5.40 \times 10^{-1}$	$[5.31-5.49] \times 10^{-1}$	$3.04 \times 10^{-4}$
FN	$r_d$	$8.82 \times 10^{-1}$	$[8.79-8.86] \times 10^{-1}$	$9.93 \times 10^{-6}$	$9.70 \times 10^{-1}$	$[9.68-9.71] \times 10^{-1}$	$1.04 \times 10^{-5}$
FN	$c$	1.62	[1.60–1.64]	$1.85 \times 10^{-4}$	1.07	[1.07–1.08]	$1.16 \times 10^{-4}$

Abbreviations: FN, full network; SB, single bifurcation; SV, single vessel.

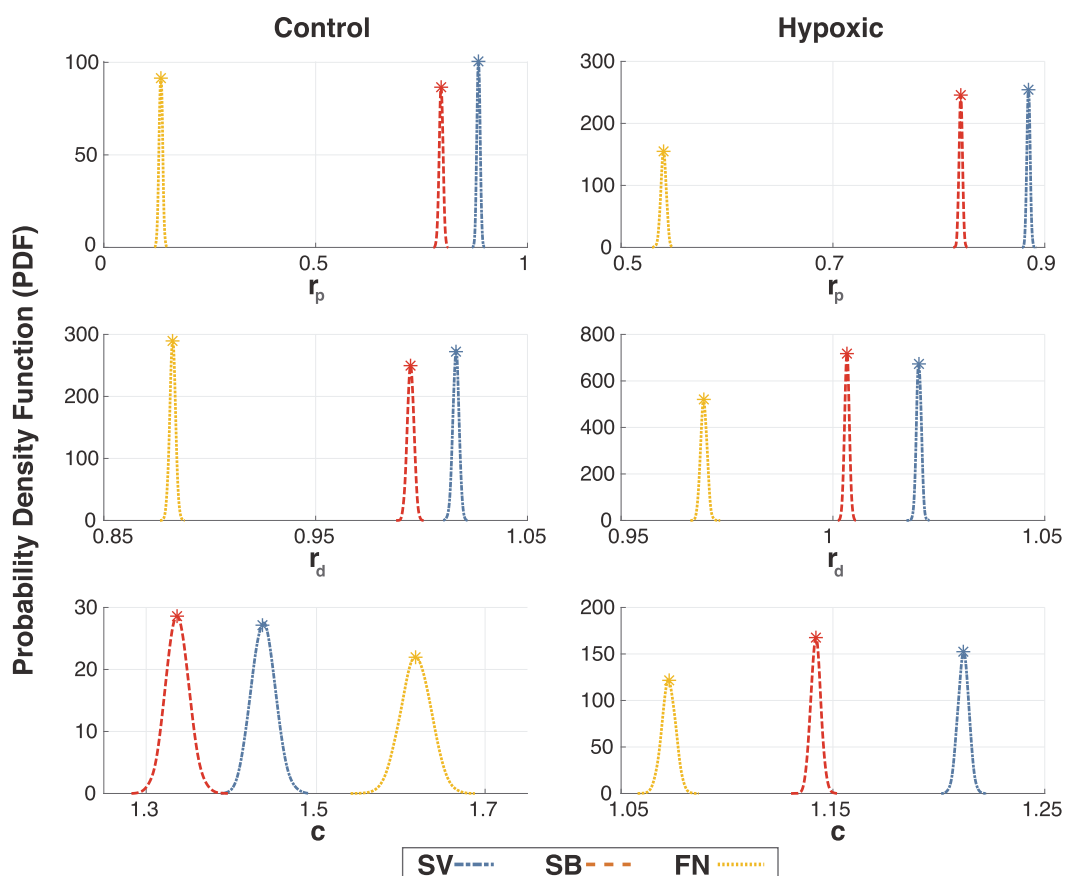


**FIGURE 9** Posterior densities obtained from 10 000 chain iterations of Delayed Rejection Adaptive Metropolis (DRAM) from the single vessel (SV) (dash-dot, blue curve), single bifurcation (SB) (dashed, red curve), and full network (FN) (dotted, yellow curve) models for the control and hypoxic mice. Graphs show results after discarding the 2000 iteration burn-in period. The parameter values obtained from the sequential quadratic programming (SQP) optimization are plotted with asterisks on the density curves. Values on the abscissa denote the parameter values for the respective scaling factors

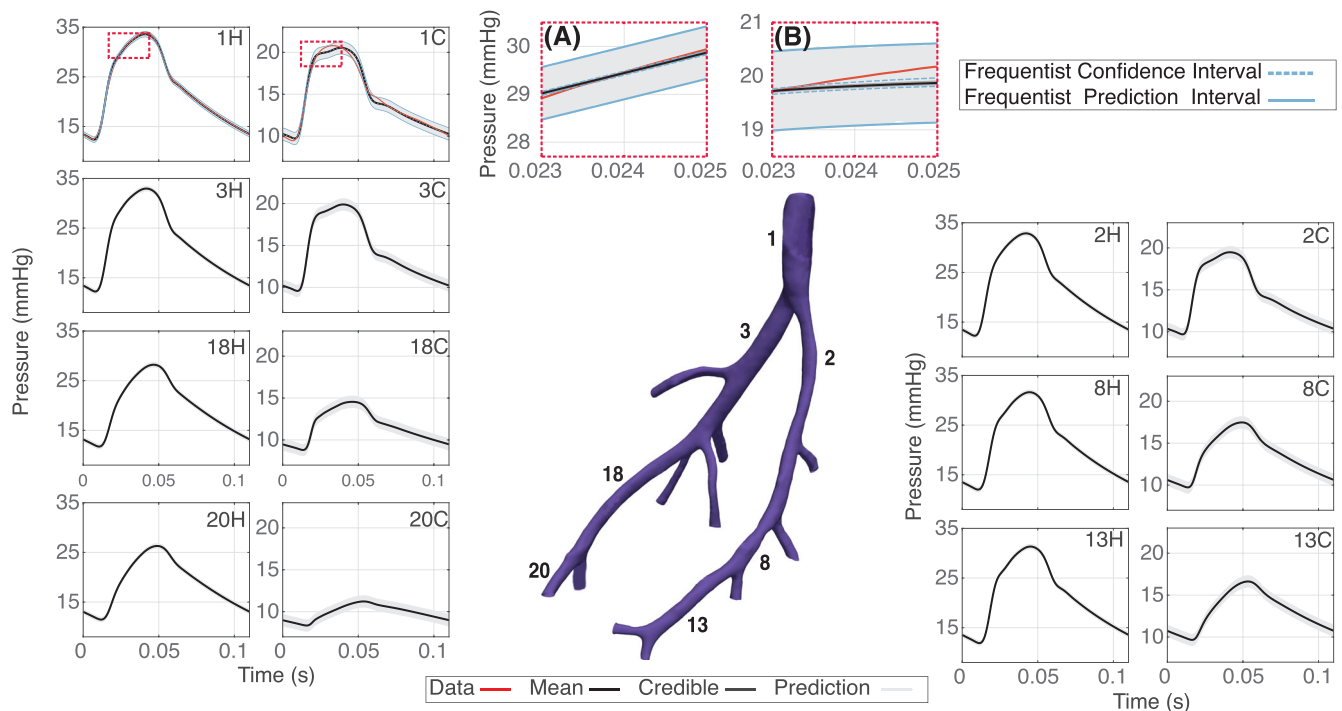


**FIGURE 10** Main pulmonary artery (MPA) pressure uncertainty in the proximal and downstream vasculature computed using frequentist and Bayesian techniques. For each vessel, pressure predictions in the left column are for the control mouse (denoted by a C) while the right column shows pressure predictions in the hypoxic mouse (denoted by an H). Panels A and B show a zoom during systole, illustrating that the frequentist analysis agrees with Bayesian estimates and that the data lies within the uncertainty bounds. These panels show that the uncertainty bounds are wider for the control mouse than the hypoxic mouse agreeing with observations that the hypoxic model fits the data better

Results show that the maximum a posteriori (MAP) parameter value corresponding to the maximum value of the posterior density aligns with the SQP optimization results and that the posterior distributions are unimodal, indicating an agreement between frequentist and Bayesian methodologies. This is also observed in Figure 8, as the frequentist and Bayesian parameter estimates (panels (c),(d) and (e),(f), respectively) produce nearly identical predictions of MPA pressure. The width of the parameter posteriors, calculated from the variance of the distribution  $\sigma_\theta^2$  are larger for the control models than for the hypoxic models (shown in Table 5). This result is similar to the frequentist analysis, as the larger residual for the control prediction leads to wider parameter confidence intervals. The width of the posterior distributions agree with the sensitivity analysis results; the variance of the compliance posterior is largest, indicating a smaller influence on MPA pressure, while proximal and distal resistance have a smaller posterior. The variance estimates for each parameter are given in Table 5.

Bayesian credible and prediction intervals for MPA pressure are constructed by drawing 2000 realizations from the parameter posterior densities. The confidence, prediction, and credible intervals for MPA pressure predictions are shown in Figure 10 using the FN model. Results show that the frequentist and Bayesian intervals agree and that the data lies within the confidence bounds. Similar results are obtained for the SV and SB models, yet it should be noted that intervals are larger in the control mouse than the hypoxic, indicating a greater uncertainty in control, MPA predictions.

#### 4.5 | Network predictions

Figure 8 illustrates that all three models can predict nearly identical dynamics in the MPA. However, both the SV and SB models cannot predict pressure multiple generations away from the MPA, while with the FN model we can predict pressure in all 21 vessels. We constructed Bayesian credible and prediction intervals to understand how parameter uncertainty affects pressure predictions distal to the MPA. Figure 10 shows the pressure data in the MPA compared with

frequentist and Bayesian prediction intervals, along with uncertainty bounds for seven vessels in the FN model for both the control and hypoxic mouse.

Model predictions in vessels immediately distal to the MPA retain a similar systolic and pulse pressure (the difference between the maximum and minimum pressure) as the MPA. In contrast, the distal vessel predictions show a decreased pulse pressure, especially in the control mouse. The pulse pressure decreased by 68% in the control vs 28% in the hypoxic mouse, indicating larger pressure attenuation in the control mouse.

## 5 | DISCUSSION

This study investigates how the behavior of a 1-D fluids model changes with network size and pathology. We used local and global sensitivity analysis to determine parameter influence and model sensitivity under different network sizes and then used local correlation analysis and MCMC pairwise plots to quantify parameter correlations. Subsequently, we used parameter inference and uncertainty quantification to identify optimal parameter values and study the effects of inherent parameter uncertainty. Overall, our results show that the peripheral vascular resistance  $r_d$  is the most influential parameter and that the large vessel stiffness  $\beta$  increases in influence with network size, while the model sensitivity to peripheral vascular compliance  $c$  and resistance  $r_p$  decreases with network size.

### 5.1 | Sensitivity ranking

The three representative networks (SV, SB, and FN) studied here contain different 1-D to 0-D model ratios. Figure 6 shows that the proximal vessel stiffness  $\beta$  becomes more influential in determining model dynamics as more vessels are added to the network. As we add more vessels, we approximate less of the downstream vasculature via Windkessel models, hence minimizing their influence on MPA predictions. Specifically, the scaling factors  $r_p$  and  $c$  become less influential, especially in the hypoxic mouse, suggesting that inferring the proximal vessel stiffness is more important than inferring parameters describing the periphery. The one exception to this is the control mouse compliance, which is ranked more influential by the global analysis because of the large nonlinear/interaction effects. The compliance plays a larger role in the control mouse because the large vessels are less stiff (i.e.,  $\beta$  is smaller), which makes compliance more influential in determining the magnitude of the pressure waves in the MPA. These results suggest that larger networks encompassing more of the pulmonary arteries may be less sensitive to changes in proximal resistance, i.e., it may be possible to fix  $R_p$  at each terminal vessel or use simpler boundary conditions.

Quantifying the influence of the Windkessel parameters can assist in understanding which parameters provide more information for the optimization routine, especially when the dimensionality of the network is large compared with the amount of data available. Similar to previous findings,<sup>39</sup> the high influence of  $R_d$  suggests that more explicit modeling of the peripheral vasculature may be beneficial in minimizing the uncertainty in pressure predictions. Moreover, the number of vessels in the model dictates how influential Windkessel parameters are, which ultimately can lead to changes in inferred parameters. From a clinical perspective, this can change the interpretation of PH altering hypothesized treatment strategies, e.g., targeted pharmaceutical therapies<sup>1</sup> as regions of high distal resistance (i.e.,  $R_d$ ) might change with network size. Overall, the local and global sensitivity methods give similar parameter rankings, as shown in Figure 6, suggesting that the local sensitivity analysis, which is less computationally expensive, provides accurate information about the model sensitivity.

### 5.2 | Time-varying sensitivities

As depicted in Figure 4, the parameter  $\beta$  has the largest effect on pressure predictions during systole, where the volume changes are the largest, thereby increasing vessel strain and blood pressure. These results are similar to the findings by Xiu et al<sup>27</sup> who showed that pressure wave reflections returning at peak systole are affected by vessel stiffness. The proximal resistance,  $\hat{R}_p = \hat{r}_p R_p$ , has a maximum influence aligned with the peak systolic pressure in the SV model. However, in the FN model, the maximum influence is shifted toward the start of systole for the control mouse and is near the end of systole in the hypoxic mouse. This suggests that both the large artery stiffness and proximal downstream resistance have an immediate effect on the pressure for the SV model, but that their effect on larger network pressure predictions are altered due to an increase in network size. Similarly, the maximum and minimum of

the model sensitivity to compliance shifts when adding vessels to the system. One possible explanation is that adding more vessels to the network introduces new impedance mismatches at vessel junctions and at the boundary, introducing wave reflections in the model predictions. This in turn alters the propagation of pressure downstream, since changes in model parameters now change model dynamics distal to the MPA. A more advanced sensitivity metric, such as a time-averaged Sobol' index<sup>36</sup> may better indicate how global sensitivities are changing with network size and over the cardiac cycle.

The peripheral resistance  $\hat{R}_d = \hat{r}_d R_d$  has the largest influence on pressure during diastole and shows decreased influence during systole, obtaining its largest values during periods of minimal flow. Physiologically, we expect that distal vascular resistance should be the most influential parameter during diastole, as this would indicate a greater diastolic pressure maintained due to higher resistance to flow downstream. This result agrees with the previous studies<sup>26,39</sup> in the systemic circulation which showed that the influence of boundary resistance was greatest during diastole. The model sensitivity to compliance oscillates between systole and diastole, but decreases for an increased number of vessels in the system, indicating a stronger dominance of model behavior from 1-D model parameters (i.e.,  $\beta$ ).

### 5.3 | Parameter inference

The 1-D models presented here include at most 21 vessels with 11 terminal vessels (giving 21 stiffness parameters  $\beta$  and 33 outlet boundary conditions). As discussed in the methods section, resistors and capacitors in series and parallel are unidentifiable and highly correlated, making it nearly impossible to estimate individual outlet parameters without additional data.<sup>23,24,62-64</sup> To remedy this issue, we introduced scaling factors  $r_p$  and  $r_d$  for the proximal and distal resistance ( $R_p$  and  $R_d$ ) and  $c$  for the total peripheral compliance ( $C$ ). We argue that this method of parameter reduction is advantageous in comparison with traditional subset reduction techniques or parameter fixing<sup>20,24,64</sup> because it allows us to tune all boundary condition parameters without having large dimensionality in our parameter space. If additional data are available downstream, e.g., in the left and right pulmonary artery, scaling factors may be identified for each distal vascular bed.

Both the correlation analysis and the DRAM posteriors showed that the hypoxic parameter set had significant correlations between  $\beta$  and  $r_p$  ( $|v_{ij}| > 0.95$  vs  $|v_{ij}| > 0.85$  for the control mouse). We chose to fix  $\beta$  at a constant value for control and hypoxic mice across all three models, i.e., we set up an optimization scheme where we inferred a common value of  $\beta$  in each mouse along with estimates of  $r_p, r_d, c$  for each network size. This is common in previous pulmonary modeling studies<sup>15,44,60,61</sup> which provided physiological results using a fixed, vessel-independent stiffness. The agreement between local and global correlation analysis reinforces the idea that the computationally cheaper local analysis can assist in parameter reduction before performing any global, Bayesian analysis.<sup>45,64,67</sup>

For the Bayesian parameter inference (DRAM) we kept  $\beta$  constant at the optimized value, allowing for better construction of the scaling factor parameter posterior distributions. Results show that the hypoxic mouse has a lower peripheral compliance than the control mouse.<sup>17,44</sup> An interesting observation is the ratio of proximal to total resistance (i.e.,  $R_p/R_T$ ) is nearly the same between disease type in the SV and SB model, but the control FN model shows a drastic reduction in the ratio (0.04, see Table 3). Moreover, the total resistance for all three models in each disease type is well approximated by the nominal values, whereas the compliance estimates for the control mouse are much larger than the nominal values. The increased value of  $c$  is likely due to an inability to capture the exact dynamics of the control data, indicating more complex vascular wall mechanics and inviting further investigation into complex constitutive equation.<sup>11-14,17</sup>

The DRAM and uncertainty quantification results support the frequentist analysis results. The overlap between the MAP estimates and the frequentist estimates, as well as the uni-modality of the posterior distributions, indicates that no other local minima exist within the parameter bounds sampled. Frequentist optimization takes significantly less computation time (on the order of hours) compared to a Bayesian analysis like DRAM (on the order of weeks), which encourages the use of frequentist analysis. However, the parameter posteriors provided from DRAM can be used to quantify uncertainty without performing asymptotic analysis, making it a more robust estimate of parametric uncertainty. Likewise, the prediction intervals indicate that both the control and hypoxic models have minimal uncertainty in MPA predictions, as the 95% prediction intervals reveal a  $\pm 1\text{-mmHg}$  band around the mean prediction. Further analysis of the parameter distributions showed that the control mouse has wider bands of uncertainty due to the larger data misfit.

## 5.4 | Physiological insight

The pulmonary circulation consists of an expansive network of blood vessels, which branch in rapid succession from the MPA to the capillaries, encapsulating the alveoli. It is known that the distal pulmonary vasculature is modulated by disease, both structurally by changing the network morphometry<sup>1,15</sup> and materially by changing vessel stiffness.<sup>14,48,53</sup> Current classification of PH and its progression is based on assessing if the pathophysiology is located in the proximal or peripheral vasculature. A model for a specific PH etiology may only require the proximal arteries (e.g., for studying blood flow in the first pulmonary bifurcation<sup>4</sup>) or might require analysis of dynamics in the entire network, e.g., modeling the influence of downstream thrombosis in chronic thromboembolic PH (CTEPH) on MPA dynamics.<sup>73</sup> Our results indicate that models of different complexity can provide similar predictions of pressure, but are influenced differently by their physiological parameters. This provides insight into how to develop a multi-scale model that can distinguish characteristics of proximal pulmonary arteries and those of downstream, distal segments. Optimization results (shown in Table 4) show that parameters inferred in the hypoxic mouse provide a better fit to data than those inferred for the control mouse. We hypothesize that this is due to stiffer vessels in the hypoxic model, leading to smaller and more linear area deformation. This makes the linear wall model more appropriate for describing the vessel deformation. Conversely, the control model does not provide as accurate of a fit, likely due to the high compliance in the pulmonary tissue, inducing complex dynamics. This agrees with previous findings<sup>12-14</sup> that arterial vessel deformation is nonlinear and viscoelastic in healthy controls. Finally, results from the optimization indicate that the control FN model can better describe the dynamics *in vivo* than the SV and SB model. The addition of terminal vessels in the system allows for more accurate calibration of the network compliance. However, the hypoxic model best fits the data when only using the SV model, though the magnitude of the cost is of similar magnitude for the SB and FN models.

It is not obvious how to distinguish between “large” and “small” peripheral vessels, making it difficult to determine the cutoff between explicit and lumped representation of the vasculature. Three previous studies<sup>26,33,43</sup> have examined how model predictions and parameter influence may change when reducing the size of the vascular network in the systemic circulation, showing that model predictions converge at a certain number of vessels. To our knowledge, no previous studies have analyzed the pulmonary circulation in this manner. When using a model of this type for analyzing clinical data, it may not be advantageous to use the simplest possible model, especially when studying disease progression and global network remodeling. For example, the SV network is able to match data in the MPA, but it cannot predict pressure and flow in the distal pulmonary branches, essential when studying the progression PH. This point was discussed by Kheyfets et al,<sup>73</sup> who highlighted the importance of network size by showing a change in predicted distal wall shear stress due to a change in distal vascular geometry. Moreover, wave propagation cannot be analyzed adequately without considering downstream sites for wave reflections,<sup>16,43,74</sup> encouraging the use of larger networks. In addition, the interpretation of downstream parameter estimates changes with different networks. For example,  $R_d$  in the SV network describes the distal resistance of the entire downstream vasculature, while  $R_d$  in larger network models describes the lumped vascular resistance immediately distal to the terminal vessels, providing a more specific location for the downstream resistance. While this study used at most 21 vessels in the model, a more detailed network with hundreds of pulmonary blood vessels can provide a more detailed description of downstream dynamics.<sup>4,73</sup> In summary, this study reveals that characteristics of the model (i.e., model sensitivity to changes in parameter values) change in larger networks, encouraging the use of network complexity that best answers the physiologically hypothesis in question. Moreover, the incorporation of a 1-D fluids model in clinical decision making must utilize the fact that uncertainties arise when hemodynamic data and image resolution are limited.

## 5.5 | Limitations

A limitation of this analysis is that we did not consider the variation in network dimensions within disease type, nor did we account for the uncertainties in topology associated with inaccurate image segmentation. Previous studies have shown that the uncertainty in dimensions can be significant,<sup>26,35,39,41,74</sup> for instance, in the prediction of coronary dynamics around a blockage.<sup>41,75</sup> However, this analysis has not been done in the case of the pulmonary circulation, which may be critical if modeling flow through clotted vessels in chronic thromboembolic PH patients.<sup>1,16,73</sup> These results do not account for the uncertainty in measured inflow, which has been addressed previously<sup>38</sup> and can be accounted for using techniques such as Karhunen-Loeve expansions, allowing for discrete representations of continuous random-fields. We hypothesize that the inflow profile is highly influential in predictions of pressure in the pulmonary

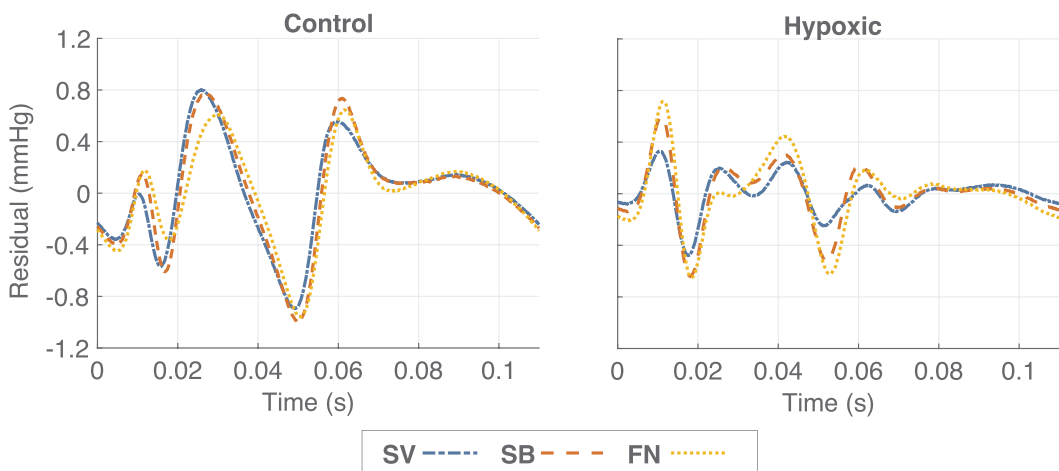


**FIGURE 11** Residuals from the model predictions with the optimized parameters. The residual curves indicate that errors are not independent, violating the simplifying assumptions often made about physical models when performing parameter inference

system; however, this analysis is beyond the scope of the current study. Similar to previous studies,<sup>15,16,61</sup> we assume that the vessel stiffness is constant throughout the network. However, Lee et al<sup>14</sup> showed that the stiffness of the proximal pulmonary arteries is heterogeneous in control mice, yet this change in stiffness has little effect on pressure predictions. In the case of PH, vascular stiffness may be vessel dependent at early stages of the disease and can provide insight into which vessels are the largest contributors to increased MPA pressure. In addition, the assumption of constant arterial stiffness may break down if small arteries or arterioles are included in the model. This could be addressed by having an adaptive, nonconstant vessel stiffness.<sup>8,12,14,15</sup> Performing a sensitivity analysis on this function may provide a radius dependent model sensitivity to vascular stiffness.

The assumption of iid errors is often made for simplicity when defining the likelihood function (Equation 24) for MCMC routines, yet a plot of the residuals in Figure 11 shows that the residuals are not independent, as indicated by the oscillatory behavior. In future studies, we propose to address this, e.g., by employing a log-likelihood  $\log(\mathcal{L})$ , defined as

$$\log(\mathcal{L}) = -\frac{1}{2}\log(\det(2\pi\Sigma)) - \frac{1}{2}\chi^T\Sigma^{-1}\chi, \quad (26)$$

where  $\Sigma$  is the covariance matrix between the data points of the time series.

The results presented here depend on the model analyzed and data available for model validation. Another limitation in this work is the inability to verify downstream predictions, as data is only measured in the MPA. If more data are available, which is typically the case in systemic cardiovascular disease,<sup>4,6,7,33,43,76</sup> more parameters may be inferred. Moreover, physiological constraints, such as assumptions of a non-negligible pressure drop, could be enforced to increase the number of identifiable parameters. Larger networks encompassing arterioles could have variable viscosity due to Fahraeus Lindqvist effect,<sup>77</sup> which could be addressed using the method proposed in this study. Finally, since this study used existing data, we were not able to study if changes in sampling rate impact model predictions.

## 6 | CONCLUSION

The objective of this study is to analyze the sensitivity and uncertainty of a coupled 1-D0-D model of pulse wave propagation in the pulmonary circulation using a new reduced parameter set. We analyzed model sensitivity and parameter correlation, inferred identifiable model parameters, determined uncertainty bounds in model predictions, and studied how changing network complexity affects parameter influence. To fit the model to data, we inferred vessel stiffness and global scaling parameters that adjust Windkessel parameters for a control and a hypoxic mouse in three networks of varying complexity. Results showed that the hypoxic mouse has stiffer vessels, with both proximal (parameterized by  $\beta$ ) and peripheral (parameterized by  $C$ ) vessels being stiffer. Moreover, we showed that distal resistance  $R_d$  has a larger influence on model predictions than other parameters and that the influence of vascular stiffness  $\beta$  increases as more vessels are added to the network. The observation that the parameters' effect on the model output (MPA pressure) varies with network complexity is essential to account for when developing models that delineate proximal vs peripheral

vascular disease. Future studies will investigate how these results play a role in human models and whether a similar analysis can be used for full models of the pulmonary circulation, including arterial and venous structures.

## ACKNOWLEDGEMENTS

We thank Prof Naomi Chesler at the University of Wisconsin, Madison for sharing the measured waveforms and micro-CT images. We thank Prof Dirk Husmeier and L. Mihaela Paun at the University of Glasgow, Scotland for their insight on Bayesian analysis. We thank Prof Ralph Smith at NC State University for discussing methodology for global sensitivity analysis. We thank Tina Ghashghaei, Apex High School for help with artwork in Figure 3. Figure 1A was modified from Servier Medical Art, licensed under a Creative Common Attribution 3.0 Generic License. <http://smart.servier.com/>. This study was supported by the American Heart Association (AHA) grant 19PRE34380459 and the National Science Foundation (NSF) grants 1615820 and 1246991.

## ORCID

Mitchel J. Colebank  <https://orcid.org/0000-0002-2294-9124>

Mette S. Olufsen  <https://orcid.org/0000-0003-2694-0044>

## REFERENCES

1. Smith LA, Kennedy JLW. *Pulmonary hypertension and related disorders*. In: *Textbook of Clinical Hemodynamics*. 2<sup>nd</sup> ed. Philadelphia, PA: Elsevier; 2018;163-181.
2. Qureshi MU, Hill NA. A computational study of pressure waves reflections in the pulmonary arteries. *J Math Biol.* 2015;71:1525-1549. <https://doi.org/10.1007/s00285-015-0867-2>
3. van de Vosse FN, Stergiopoulos N. Pulse wave propagation in the arterial tree. *Ann Rev Fluid Mech.* 2011;43:467-499. <https://doi.org/10.1146/annurev-fluid-122109-16073>
4. Bordones AD, Leroux M, Kheyfets VO, et al. Computational fluid dynamics modeling of the human pulmonary arteries with experimental validation. *Ann Biomed Eng.* 2018;46(9):1309-1324. <https://doi.org/10.1007/s10439-018-2047-1>
5. Marsden AL. Optimization in cardiovascular modeling. *Annu Rev Fluid Mech.* 2014;46:519-546. <https://doi.org/10.1146/annurev-fluid-010313-141341>
6. Alastrauey J, Parker KH, Peiro J, Sherwin SJ. Lumped parameter outflow models for 1D blood flow simulations: effect on pulse waves and parameter estimation. *Commun Comput Phys.* 2008;4:317-336.
7. Battista C, Bia D, Zocalo German Y, Armentano RL, Haider MA, Olufsen MS. Wave propagation in a 1D fluid dynamics model using pressure-area measurements from ovine arteries. *J Mech Med Biol.* 2016;16(2):1650007. <https://doi.org/10.1142/S021951941650007X>
8. Olufsen MS, Peskin CS, Kim WY, et al. Numerical simulation and experimental validation of blood flow in arteries with structured-tree outflow conditions. *Ann Biomed Eng.* 2000;28:1281-1299. <https://doi.org/10.1114/1.1326031>
9. Reymond P, Merenda F, Perren F, Rufenacht D, Stergiopoulos N. Validation of a one-dimensional model of the systemic arterial tree. *Am J Physiol.* 2009;297:H208-H222. <https://doi.org/10.1152/ajpheart.00037.2009>
10. Stergiopoulos N, Meister JJ, Westerhof N. Evaluation of methods for estimation of total arterial compliance. *Am J Physiol.* 1995;268:H1540-1548. <https://doi.org/10.1152/ajpheart.1995.268.4.H1540>
11. Raghu R, Vignon-Clementel IE, Figueroa CA, Taylor TA. Comparative study of viscoelastic arterial wall models in nonlinear one-dimensional finite element simulations of blood flow. *J Biomech Eng.* 2011;133(8):081003. <https://doi.org/10.1115/1.4004532>
12. Steele BN, Valdez-Jasso D, Haider MA, Olufsen MS. Predicting arterial flow and pressure dynamics using a 1D fluid dynamics model with a viscoelastic wall. *SIAM J Appl Math.* 2011;71:1123-1143. <https://doi.org/10.1137/100810186>
13. Valdez-Jasso D, Bia D, Zcalo Y, et al. Linear and nonlinear viscoelastic modeling of aorta and carotid pressure-area dynamics under in vivo and ex vivo conditions. *Ann Biomed Eng.* 2011;39:1438-1456. <https://doi.org/10.1007/s10439-010-0236-7>
14. Lee P, Carlson BE, Chesler N, et al. Heterogeneous mechanics of the mouse pulmonary arterial network. *Biomech Model Mechanobiol.* 2016;15(5):1245-1261. <https://doi.org/10.1007/s10237-015-0757-y>
15. Olufsen MS, Hill NA, Vaughan GD, Sainsbury C, Johnson M. Rarefaction and blood pressure in systemic and pulmonary arteries. *J Fluid Mech.* 2012;705:280-305. <https://doi.org/10.1017/jfm.2012.220>
16. Qureshi MU, Vaughan GD, Sainsbury C, et al. Numerical simulation of blood flow and pressure drop in the pulmonary arterial and venous circulation. *Biomech Model Mechanobiol.* 2014;13:1137-1154. <https://doi.org/10.1007/s10237-014-0563-y>
17. Qureshi MU, Colebank MJ, Paun M, et al. Hemodynamic assessment of pulmonary hypertension in mice: a model based analysis of the disease mechanism. *Biomech Model Mechanobiol.* 2019;18:219-243. <https://doi.org/10.1007/s1023>

18. McDonald DA, Attinger EO. The characteristics of arterial pulse wave propagation in the dog. *Inform Exch Gp. No 3. Sci Mem.* 1965;7.
19. Eck VG, Donders WP, Sturdy J, et al. Advances in 0D and 1D models for circulation: a guide to uncertainty quantification and sensitivity analysis for cardiovascular applications. *Int J Numer Meth Biomed Eng.* 2016;e02755:32. <https://doi.org/10.1002/cnm.2755>
20. Ellwein LM, Tran HT, Zapata C, Novak V, Olufsen MS. Sensitivity analysis and model assessment: mathematical models for arterial blood flow and blood pressure. *Cardiovasc Eng.* 2008;8:94-108. <https://doi.org/10.1007/s10558-007-9047-3>
21. Morris MD. Factorial plans for preliminary computational experiments. *Technometrics.* 1991;33:161-174.
22. Saltelli A, Ratto M, Andres T, et al. Global Sensitivity Analysis The primer: John Wiley and Sons, Chichester UK; 2008.
23. Smith RC. *Uncertainty Quantification Theory, Implementation, and Applications.* Philadelphia PA: SIAM; 2014.
24. Olsen CH, Ottesen JT, Smith RC, Olufsen MS. Parameter subset selection techniques for problems in mathematical biology. *Biol Cybern.* 2018;1-18. <https://doi.org/10.1007/s00422-018-0784-8>
25. Alexanderian A, Gremaud PA, Smith RC. Variance-based sensitivity analysis for time-dependent processes. *arXiv Preprint.* 2017;1711:08030.
26. Melis A, Clayton RH, Marzo A. Bayesian sensitivity analysis of a 1D vascular model with Gaussian process emulators. *Int J Numer Method Biomed Eng.* 2017;e2882:33. <https://doi.org/10.1002/cnm.2882>
27. Xiu D, Spencer SJ. Parametric uncertainty analysis of pulse wave propagation in a model of a human arterial network. *J Comput Phys.* 2007;226:1385-1407. <https://doi.org/10.1016/j.jcp.2007.05.020>
28. Iott J, Haftka RT, Adelman HM. Selecting step sizes in sensitivity analysis by finite differences NASA-TM-86382; 1985.
29. Griewank A. On automatic differentiation. In: Iri M. and Tanabe K., (eds.), *Mathematical Programming: Recent Developments and Applications.* Kluwer, Dordrecht, the Netherlands; 1989:83-108.
30. Banks HT, Bekele-Maxwell K, Bociu L, Noorman M, Tillman K. The complex-step method for sensitivity analysis of non-smooth problems arising in biology. *Eurasian J Math Comput Appl.* 2015;3:15-68.
31. Campolongo F, Cariboni J, Saltelli A. An effective screening design for sensitivity analysis of large models. *Environ Model Softw.* 2007;22:1509-1518. <https://doi.org/10.1016/j.envsoft.2006.10.004>
32. Wentworth MT, Smith RC, Banks HT. Parameter selection and verification techniques based on global sensitivity analysis illustrated for an HIV model. *SIAM/ASA J Uncert Quant.* 2016;4:266-297. <https://doi.org/10.1137/15M1008245>
33. Epstein S, Willemet M, Chowienczyk PJ, Alastrauey J. Reducing the number of parameters in 1D arterial blood flow modeling: less is more for patient-specific simulations. *Am J Physiol.* 2015;309:H222-H234. <https://doi.org/10.1152/ajpheart.00857.2014>
34. Karau K, Johnson R, Molthen R, et al. Microfocal X-ray CT imaging and pulmonary arterial distensibility in excised rat lungs. *Am J Physiol.* 2011;281:H1447-H1457. <https://doi.org/10.1152/ajpheart.2001.281.3.H1447>
35. Moore JA, Steinman DA, Ethier CR. Computational blood flow modelling: errors associated with reconstructing finite element models from magnetic resonance images. *J Biomech.* 1998;31(2):179-184.
36. Eck VG, Sturdy J, Hellevik LR. Effects of arterial wall models and measurement uncertainties on cardiovascular model predictions. *J Biomech.* 2016;50:188-194. <https://doi.org/10.1016/j.jbiomech.2016.11.042>
37. Arnold A, Battista C, Bia D, et al. Uncertainty quantification in a patient-specific 1D arterial network model: EnKF-based Inflow estimator. *J Verif Valid Uncert.* 2017;011002:2. <https://doi.org/10.1115/1.4035918>
38. Brault A, Dumas L, Lucor D. Uncertainty quantification of inflow boundary condition and proximal arterial stiffness coupled effect on pulse wave propagation in a vascular network. *Int J Numer Method Biomed Eng.* 2016;e2859:33. <https://doi.org/10.1002/cnm.2859>
39. Chen P, Quarteroni A, Rozza G. Simulation-based uncertainty quantification of human arterial network hemodynamics. *Int J Numer Meth Biomed Eng.* 2013;29:698-721. <https://doi.org/10.1002/cnm.2554>
40. Gul R, Schtte C, Bernhard S. Mathematical modeling and sensitivity analysis of arterial anastomosis in the arm. *Appl Math Model.* 2016;40:7724-7738. <https://doi.org/10.1016/j.apm.2016.03.041>
41. Sankaran S, Grady L, Taylor CA. Fast computation of hemodynamic sensitivity to lumen segmentation uncertainty. *IEEE Trans Med Imaging.* 2015;34:2562-2571. <https://doi.org/10.1109/TMI.2015.2445777>
42. Wu J, Dhingra R, Gambhir M, Remais JV. Sensitivity analysis of infectious disease models: methods, advances and their application. *J R Soc Interface.* 2018;20121018:10. <https://doi.org/10.1098/rsif.2012>
43. Fossan FE, Mariscal-Harana J, Alastrauey J, Hellevik LR. Optimization of topological complexity for one-dimensional arterial blood flow models. *J R Soc Interface.* 2018;15:1-16. <https://doi.org/10.1098/rsif.2018.0546>
44. Paun LM, Qureshi MU, Colebank M, et al. MCMC methods for inference in a mathematical model of pulmonary circulation. *Stat Neerl.* 2018;72(3):306-338.
45. Marquis AD, Arnold A, Dean C, Carlson BE, Olufsen MS. Practical identifiability and uncertainty quantification of a pulsatile cardiovascular model. *Math Biosci.* 2018;304:9-24. <https://doi.org/10.1016/j.mbs.2018.07.001>
46. Brady R, Frank-Ito DO, Tran HT, et al. Personalized mathematical model of endotoxin-induced inflammatory responses in young men and associated changes in heart rate variability. *Math Model Nat Phenom.* 2018;13(5). <https://doi.org/10.1051/mmnp/2018031>

47. Tabima DM, Roldan-Alzate A, Wang Z, et al. Persistent vascular collagen accumulation alters hemodynamic recovery from chronic hypoxia. *J Biomech*. 2012;45:799-804. <https://doi.org/10.1016/j.jbiomech.2011.11.020>
48. Vanderpool RR, Kim AR, Chesler NC. Effects of acute Rho kinase inhibition on chronic hypoxia-induced changes in proximal and distal pulmonary arterial structure and function. *J Appl Physiol*. 2011;110:188-198. <https://doi.org/10.1152/japplphysiol.00533.2010>
49. Feldkamp LA, Davis LC, Kress JW. Practical cone-beam algorithm. *J Opt Soc Am A*. 1984;1(6):612-619.
50. Yushkevich PA, Piven J, Hazlett HC, Smith RG, et al. User-guided 3D active contour segmentation of anatomical structures: significantly improved efficiency and reliability. *Neuroimage*. 2006;31:1116-1128. <https://doi.org/10.1016/j.neuroimage.2006.01.015>
51. Antiga L, Piccinelli M, Botti L, Ene-Iordache B, Remuzzi A, Steinman DA. An image-based modeling framework for patient-specific computational hemodynamics. *Med Biol Eng Comput*. 2008;46:1097-1112. <https://doi.org/10.1007/s11517-008-0420-1>
52. Antiga L, Steinman DA. Robust and objective decomposition and mapping of bifurcating vessels. *IEEE Trans Med Imag*. 2004;23:704-713. <https://doi.org/10.1109/TMI.2004.82694>
53. Kheyfets VO, Rios L, Smith T, Schroeder T, et al. Patient-specific computational modeling of blood flow in the pulmonary arterial circulation. *Comput Methods Programs Biomed*. 2015;120:88-101. <https://doi.org/10.1016/j.cmpb.2015.04.005>
54. Safaei S, Bradley CP, Suresh V, et al. Roadmap for cardiovascular circulation model. *J Physiol*. 2016;594:6909-6928. <https://doi.org/10.1113/JP272660>
55. Atabek HB. Wave propagation through a viscous fluid contained in a tethered, initially stressed, orthotropic elastic tube. *Biophys J*. 1968;8:626-649.
56. Acosta S, Puelz C, Rivière B, Penny DJ, Rusin CG. Numerical method of characteristics for one-dimensional blood flow. *J Comput Phys*. 2015;294:96-109. <https://doi.org/10.1016/j.jcp.2015.03.045>
57. Azer K, Peskin CS. A one-dimensional model of blood flow in arteries with friction and convection based on the Womersley velocity profile. *Cardiovasc Eng*. 2007;7:51-73.
58. Riches AC, Sharp JG, Thomas DB, Smith SV. Blood volume determination in mouse. *J Physiol*. 1973;228:279-284.
59. Windberger U, Bartholovitsch A, Plasenzotti R, Korak KJ, Heinze G. Whole blood viscosity, plasma viscosity and erythrocyte aggregation in nine mammalian species: reference values and comparison of data. *Exp Physiol*. 2003;88(3):431-440. <https://doi.org/10.1113/eph8802496>
60. Qureshi MU, Colebank MJ, Schreier DA, et al. Characteristic impedance: frequency or time domain approach? *Physiol Meas*. 2018;39(1):014004. <https://doi.org/10.1088/1361-6579/aa9d60>
61. Krenz G, Dawson C. Flow and pressure distributions in vascular networks consisting of distensible vessels. *Am J Physiol*. 2003;284:H2192-H2203. <https://doi.org/10.1152/ajpheart.00762.2002>
62. Ipsen ICF, Kelley CT, Pope SR. Rank-deficient nonlinear least squares problems and subset selection. *SIAM J Numer Anal*. 2011;49(2):1244-1266. <https://doi.org/10.1137/090780882>
63. Pironet A, Docherty PD, Dauby PC, Chase JG, Desai T. Practical identifiability analysis of a minimal cardiovascular system model. *Comput Methods Programs Biomed*. 2017;171:53-65. <https://doi.org/10.1016/j.cmpb.2017.01.005>
64. Pope S, Ellwein L, Zapata C, et al. Estimation and identification of parameters in a lumped cerebrovascular model. *Math Biosci Eng*. 2009;6(1):93-115. <https://doi.org/10.3934/mbe.2009.6.93>
65. Hasenauer J, Allgöwer F, Waldherr S, Wagner K. Parameter identification, experimental design and model falsification for biological network models using semidefinite programming. *IET Syst Biol*. 2010;4(2):119-130. <https://doi.org/10.1049/iet-syb.2009.0030>
66. Sumner T, Shephard E, Bogle IDL. A methodology for global-sensitivity analysis of time-dependent outputs in systems biology modelling. *J R Soc Interface*. 2012;9:2156-2166. <https://doi.org/10.1098/rsif.2011.0891>
67. Olsen C, Tran H, Ottesen JT, Mehlsen J, Olufsen M. Challenges in practical computation of global sensitivities with application to a baroreceptor reflex model. NC State University, Center for Research in Scientific Computation. CRSC-TR13-15; 2013.
68. Banks HT, Cintron-Arias A, Kappel F. Parameter selection methods in inverse problem formulation. In: *Mathematical Modeling and Validation in Physiology, Lecture Notes in Math*. 2064, Heidelberg: Springer; 2013:43-73. [https://doi.org/10.1007/978-3-642-32882-4\\_3](https://doi.org/10.1007/978-3-642-32882-4_3)
69. Olufsen MS, Ottesen JT. A practical approach to parameter estimation applied to model predicting heart rate regulation. *J Math Biol*. 2013;67:39-68. <https://doi.org/10.1007/s00285-012-0535-8>
70. Haario H, Laine M, Mira A, Saksman E. DRAM: Efficient adaptive MCMC. *Stat Comput*. 2006;16:339-354. <https://doi.org/10.1007/s11222-006-9438-0>
71. Laine M. MCMC Toolbox for Matlab. <http://helios.fmi.fi/lainema/dram/>. Accessed May 10, 2018.; 2007.
72. Geweke J. Evaluating the accuracy of sampling-based approaches to the calculation of posterior moments. *Bayes Stat*. 1992;4:169-193.
73. Kheyfets VO, O'Dell W, Smith T, Reilly JJ, Finol EA. Considerations for numerical modeling of the pulmonary circulation: a review with a focus on pulmonary hypertension. *J Biomech Eng*. 2013;061011:135. <https://doi.org/10.1115/1.4024141>
74. Leguya CAD, Bosboom EMH, Belloum ASZ, Hoeks APG, van de Vosse FN. Global sensitivity analysis of a wave propagation model for arm arteries. *Med Eng Phy*. 2011;33:1008-1016. <https://doi.org/10.1016/j.medengphy.2011.04.003>
75. Ellwein LM, Marks DS, Migrino RQ, et al. Image-based quantification of 3D morphology for bifurcations in the left coronary artery: application to stent design. *Catheter Cardiovasc Interv*. 2016;87:1244-1255. <https://doi.org/10.1002/ccd.26247>

76. Mynard JP, Smolich JJ. One-dimensional haemodynamic modeling and wave dynamics in the entire adult circulation. *Ann Biomed Eng*. 2015;43:1443-1460. <https://doi.org/10.1007/s10439-015-1313-8>
77. Lighthill SJ. *Mathematical Biofluid Dynamics*. Philadelphia: PA; SIAM; 1975.

**How to cite this article:** Colebank MJ, Qureshi MU, Olufsen MS. Sensitivity analysis and uncertainty quantification of 1-D models of pulmonary hemodynamics in mice under control and hypertensive conditions. *Int J Numer Meth Biomed Engng*. 2021;37:e3242. <https://doi.org/10.1002/cnm.3242>

## APPENDIX A

The Delayed Rejection Adaptive Metropolis (DRAM) algorithm, outlined in Smith,<sup>23</sup> is detailed in Algorithm 1 below and implemented using the DRAM software in MATLAB.<sup>71</sup> For brevity, we assume our errors are normal, independent, and identically distributed, allowing us to define the posterior density of the parameters  $\theta$  conditioned on the data  $p_{\text{data}}$  as  $\pi(\theta|p_{\text{data}}) = \frac{e^{-SS_\theta/2\sigma^2}}{(2\pi\sigma^2)^{N/2}}$  where  $SS_\theta = \chi^T(\theta)\chi(\theta)$ , and  $N$  is the number of data points. The traditional Metropolis algorithm incorporates an acceptance probability  $\alpha$  for the candidate parameter  $\theta_{\text{cand}}$  conditioned on the  $(k-1)$ -th accepted parameter

$$\alpha(\theta_{\text{cand}}|\theta_{k-1}) = \min\left(1, \frac{\pi(\theta_{\text{cand}}|p_{\text{data}})}{\pi(\theta_{k-1}|p_{\text{data}})}\right) = \min\left(1, e^{-(SS_{\text{cand}} - SS_{k-1})/2s_{k-1}^2}\right), \quad (\text{B1})$$

where  $J(\theta_{\text{cand}}|\theta_{k-1})$  is the proposal distribution for the new parameter value, which is assumed to be a multivariate, normal distribution with covariance  $V$ .

The delayed rejection (DR) component of the DRAM algorithm considers a second candidate parameter  $\theta_{\text{DR}}$  if the first candidate parameter  $\theta_{\text{cand}}$  is not accepted. The second parameter is chosen as described in Algorithm 1 and is accepted using the second acceptance probability

$$\begin{aligned} \alpha_{\text{DR}}(\theta_{\text{DR}}|\theta_{\text{cand}}, \theta_{k-1}) &= \min\left(1, \frac{\pi(\theta_{\text{DR}}|p_{\text{data}}) J(\theta_{\text{cand}}|\theta_{\text{DR}}) J(\theta_{k-1}|\theta_{\text{DR}}, \theta_{\text{cand}})}{\pi(\theta_{k-1}|p_{\text{data}}) J(\theta_{\text{cand}}|\theta_{k-1}) J(\theta_{\text{DR}}|\theta_{k-1}, \theta_{\text{cand}})} \frac{1 - \alpha(\theta_{\text{cand}}|\theta_{\text{DR}})}{1 - \alpha(\theta_{\text{cand}}|\theta_{k-1})}\right) \\ &= \min\left(1, \frac{\pi(\theta_{\text{DR}}|p_{\text{data}}) J(\theta_{\text{cand}}|\theta_{\text{DR}})}{\pi(\theta_{k-1}|p_{\text{data}}) J(\theta_{\text{cand}}|\theta_{k-1})} \frac{1 - \alpha(\theta_{\text{cand}}|\theta_{\text{DR}})}{1 - \alpha(\theta_{\text{cand}}|\theta_{k-1})}\right), \end{aligned} \quad (\text{B2})$$

where we employ the fact that the proposal distribution  $J(\theta_{\text{DR}}|\theta_{k-1}, \theta_{\text{cand}})$  is symmetric and can be cancelled from the original fraction. Lastly, the adaptive Metropolis (AM) component of the algorithm is used to assist in avoiding random walk behavior in Markov chain Monte Carlo (MCMC) sampling when dealing with correlated parameters by updating the parameter covariance according to a multivariate, normal distribution. The covariance is adapted using previous parameter values after some adaptation length  $k_0$ ,

$$V_k = \begin{cases} V_{k-1} & \text{if } k < k_0 \\ s_P \text{cov}(\theta_0, \theta_1, \dots, \theta_{k-1}) + \epsilon \mathcal{I}_P & \text{if } k = k_0, \end{cases} \quad (\text{B3})$$

where  $P$  is the number of parameters in the model,  $s_P$  is a design parameter that depends on the dimension of the parameter vector,  $\mathcal{I}_P$  is the  $P \times P$  identity matrix, and  $\epsilon \geq 0$  is a small perturbation parameter to ensure that  $V_k$  is positive definite. A common choice is  $s_P = 2.38^2 P$ , which is used in the DRAM package considered in this text.<sup>71</sup>

**Algorithm 1** Delayed Rejection Adaptive Metropolis (DRAM) algorithm

1. Define the DRAM design parameters: the number of observations encoded in the prior  $n_s (= 1)$ ; the mean squared error of the observations  $\sigma_s^2$ ; the length of the adaptation interval before updating the covariance  $k_0 (= 100$  steps); the number of chain iterations before terminating  $M$
2. Compute  $\theta_0 = \arg \min_{\theta} [\chi^T(\theta)\chi(\theta)]$ , where  $\chi(\theta)$  is the model-data mismatch from Equation 11
3. Calculate  $SS_0 = \chi^T(\theta_0)\chi(\theta_0)$  and set the initial variance estimate as  $s_0^2 = \frac{SS_0}{N-P}$
4. Determine initial covariance estimate  $V = s_0^2 [S^T(\theta_0)S(\theta_0)]^{-1}$  and the Cholesky factorization  $R = \text{Chol}(V)$
5. **for**  $i = 1, 2, \dots, M$ 
  - (a) Draw a sample  $\xi_k \sim \mathcal{N}(0, 1)$  and compute candidate parameter  $\theta_{\text{cand}} = \theta_{k-1} + R\xi_k$
  - (b) Draw a uniform random sample  $u_\alpha \sim U(0, 1)$
  - (c) Set  $SS_{\text{cand}} = \chi^T(\theta_{\text{cand}})\chi(\theta_{\text{cand}})$
  - (d) Calculate the acceptance probability  $\alpha(\theta_{\text{cand}} | \theta_{k-1}) = \min\left(1, e^{-(SS_{\text{cand}} - SS_{k-1})/2s_{k-1}^2}\right)$
  - (e) **if**  $u_\alpha < \alpha$ 
    - (i) Set  $\theta_k = \theta_{\text{cand}}$  and  $SS_k = SS_{\text{cand}}$
  - else (Delayed Rejection)**
    - (i) Set  $\gamma_2 = \frac{1}{5}$  and sample  $\xi_k \sim \mathcal{N}(0, 1)$
    - (ii) Construct second-state candidate  $\theta_{\text{DR}} = \theta_{k-1} + \gamma_2 R\xi_k$  and draw the sample  $u_{\text{DR}} \sim U(0, 1)$
    - (iii) Compute  $SS_{\text{DR}} = \chi^T(\theta_{\text{DR}})\chi(\theta_{\text{DR}})$  and acceptance probability  $\alpha_{\text{DR}}(\theta_{\text{DR}} | \theta_{\text{cand}}, \theta_{k-1})$  defined in equation (A2)
    - (iv) **if**  $u_{\text{DR}} < \alpha_{\text{DR}}$ 
      - Set  $\theta_k = \theta_{\text{DR}}$  and  $SS_k = SS_{\text{DR}}$
    - (v) **else**
      - Set  $\theta_k = \theta_{k-1}$  and  $SS_k = SS_{k-1}$
  - end if**
  - (f) Update the error variance  $s_k^2$  according to an inverse-gamma distribution, ie,  $s_k^2 \sim \text{Inv-Gamma}(a, b)$  where  $a = \frac{1}{2}(n_s + N)$  and  $b = \frac{1}{2}(n_s\sigma_s^2 + SS_k)$
  - (g) **if**  $\text{mod}(k, k_0) = 1$  (**Adaptive Metropolis**)
    - Update the covariance  $V_k = s_p \text{cov}(\theta_0, \theta_1, \dots, \theta_{k-1}) + \epsilon I_P$
  - (h) **else**
    - $V_k = V_{k-1}$
  - (i) **end if**
  - (j) Compute  $R = \text{Chol}(V_k)$
- end for**